POLITECNICO DI TORINO

**Ingegneria Energetica e Nucleare**

**Renewable energy systems**

# Self-sustained Thermo-management of Solid Oxide Fuel Cells With High Temperature Phase Change Materials

**Graduation Thesis**

**Supervisor:**

**Prof. Massimo Santarelli**

**Presented by:**

**Riccardo Gallerani**

Academic Year 2024/2025

**Abstract**

This report explores the integration of Phase Change Materials (PCMs) to maintain the temperature stability of Solid Oxide Fuel Cells (SOFCs) in maritime applications. SOFCs, known for their high efficiency and fuel flexibility, face challenges related to thermal management, especially under dynamic conditions such as load changes and shutdowns. The high operating temperatures, typically between 600°C and 1000°C, necessitate effective thermal management to prevent non-uniform thermal stresses and degradation of the cell components.

The study investigates the use of metallic PCMs (mPCMs), which offer superior thermal conductivity compared to conventional PCMs like paraffin and hydrated salts. By incorporating mPCMs into the SOFC stack, it is possible to mitigate drastic temperature variations and enhance the preheating of fuel and air inlets. It as been developed a SOFC stack modeling which involves both electrochemical and thermal modeling to predict the performance of the fuel cell. These models account for steady-state and dynamic behaviors, ensuring a comprehensive understanding of the SOFC's operation under various conditions.

Results show a significant reduction in temperature gradient during load variations. This thermal stability allows for the potential use of SOFCs in dynamic working conditions, making them a viable solution for reducing emissions in the maritime transport sector.

# Nomenclature

**ASC** Anode Supported Cell.

**ASR** Area Specific Resistance.

**BTM** Battery Thermal Management.

**CFD** Computational Fluid Dynamics.

**CSC** Cathode Supported Cell.

**CTE** Thermal Expansion Coefficient.

**EPCM** Eutectic Phase-Change Material.

**ESC** Electrolyte Supported Cell.

**GDC** Gadolinium Oxide.

**ICE** Internal Combustion Engine.

**LSGM** Lanthanum Gallate-based Materials.

**LSM** Strontium doped Lanthanum Manganite.

**LTES** Latent Thermal Energy Storage.

**mPCM** Metallic Phase-Change Material.

**PCM** Phase-Change Material.

**PEMFC** Proton Exchange Membrane Fuel Cells.

**PEN** Positive-Electrolyte-Negative Electrode Assembly.

**PM** Particulate Matter.

**SEM** Scanning Electron Microscopy.

**SOFC** Solid Oxide Fuel Cell.

**STES** Sensible Thermal Energy Storage.

**VOC** Volatile Organic Compounds.

**YSZ** Yttria Stabilized Zirconia.

# List of Figures

# List of Tables

# Index

# Chapter 1

# Introduction to SOFC systems

High temperature fuel cells are energy conversion systems capable of harnessing an electrochemical reaction between a fuel and an oxidant to produce electricity. They find application across various industrial fields, as stationary power generation, transportation and portable applications [1]. Between different typologies of high temperature fuel cells, Solid Oxide Fuel Cell (SOFC) emerges as an attractive solution and a promising technology, given the high conversion efficiency and versatility of different fuel sources [2].

These advantages come from the high operating temperature of the cell that reaches in working condition, typically between 600°C and 1000°C. It is necessary to work at high temperatures to reach adequate ionic conductivity [3]. Furthermore, the solid materials that compose the cell guarantee low cost, long theoretical life, and low maintenance cost [4]. High temperature plays also a role in the degradation mechanism of the cell due to the different thermal expansion coefficients of the materials the compose the cell itself, that can potentially lead to the failure of the cell.

Despite considering the characteristics, advantages and disadvantages of different types of high temperature fuel cell, a SOFC has been chosen for this study.

## 1.1 Characteristics of solid oxide fuel cells

The flexibility provided by the ability of the SOFCs to adapt to different kind of fuel, such as pure hydrogen, natural gas biogas, ammonia and the other hydrocarbons using carbon capture as an effective $H_2$ carrier [5, 6], is one of the characteristics that makes this type of cell particularly interesting. This flexibility is given by the high working temperature, which permits the reforming of light hydrocarbon fuels. Moreover, SOFC can be also fueled with heavier hydrocarbon fuels by implementing an external reforming [7]. In addition, SOFCs can produce exhaust gases that can also be used in a polygeneration system, for instance, by combining cooling, heating and power [5, 8].

Solid Oxide Fuel Cells show a versatility in their application being used not only for steady-state power generation but also in a more dynamic operation. However, the high temperature and heat involved in managing a dynamic response makes this type of utilization more challenging. The two primary dynamic operations that pose challenges in management are load changes and shutdown, as they can lead to issues related to cell degradation. In particular, elevated temperature and thermal gradients applied to the different materials that make up the cell, each with different thermal expansion coefficients, can induce thermal stresses that can potentially damage the materials themselves [9]. Furthermore, load changes can involve high spikes in energy demand that can be higher compared to steady-state operation [2].

## 1.2 Layout and design of SOFC

A SOFC stack is made up of many different cells that are made up of three layers: a cathode, an electrolyte, and an anode. The anode and cathode are then connected to permit the passage of electrons. Moreover, there are three different layer config-

urations that can be used, as shown in figure 1.1. The Electrolyte Supported Cell (ESC) configuration is not commonly used due to its lower power density resulting from the thick electrolyte layer [1] which increases the ohmic resistance. In contrast, in the electrode-supported cell the ohmic losses in the electrolyte are reduced due to its low thickness (around $10\eta m$) [10].

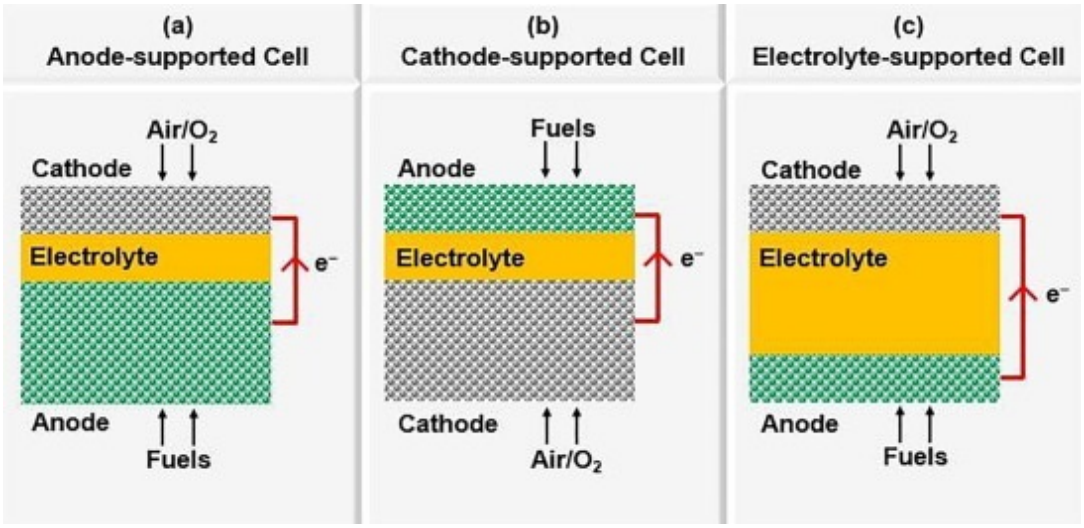


**Figure 1.1:** Configuration of anode electrolyte and cathode [1].

Due to the thin cathode, the Cathode Supported Cell (CSC) configuration can present a wide depletion zone that limits oxygen diffusion in the cathode. Because the electrochemical reaction cannot take place in the depletion zone, the effective reaction zone is reduced and so the performance. Instead, in the thick cathode of the Anode Supported Cell (ASC) configuration, the problem related with the depletion zone is than avoided [10].

Overall, the cathode-supported cell shows the highest power density, but on the contrary its high cost makes the anode-supported the best trade-off option between power density and cost. In general, the thickness of the electrolyte has the greatest influence on cell performance in comparison to that of the electrodes. Nevertheless, it is observed that a decrease of the thickness of the supporting layer leads to an increase of the cell performance [11].

The most preferred designs of SOFC are based on two different configurations, tubular or planar. A tubular design presents different advantages due to their greater tolerance to thermal cycling, quicker start-up capability since the reduced thermal stresses of the tubular geometry. However, the low power density and the fabrication process for such a geometry act as a limiting factor [1, 12]. Instead, a planar design allows for high current density and can be preferred due to simple design, easy fabrication, and cost effectiveness for commercialization [8]. However, this design pose challenges with respect to high temperature sealing and limited life attributed to reduced mechanical strength of the stack. [12].

## 1.3 Chemical reactions for energy conversion

Considering a SOFC fueled with hydrogen, it is possible to describe three different reactions that took place in the cathode and anode. On the cathode side, when the oxygen reaches the reaction zone layer, it will be reduced, as shown in Eq. (1.1). The ions of oxygen are able to pass through the electrolyte and reach the reaction zone layer of the anode, after which they react with hydrogen to produce electrons and water, as shown in Eq. (1.2). The total reaction is shown in Eq. (1.3) [11].

$$\frac{1}{2}O_2 + 2e^- \longrightarrow O^{2-} \tag{1.1}$$

$$O^{2-} + H_2 \longrightarrow H_2O + 2e^- \tag{1.2}$$

$$H_2 + \frac{1}{2}O_2 \longrightarrow H_2O \tag{1.3}$$

Another distinction that can be made is between fuel cells based on oxygen ion conductors (O-SOFC) or on proton conductors (H-SOFC). The difference stays in the electrolyte of the fuel cell, that can pass oxygen ions ($O^{2-}$) or protons ($H^+$). Considering the O-SOFC, the equation took place as described above. Instead, in H-SOFC, hydrogen will be oxidated in the anode, as in Eq. (1.4). Therefore, the

product of the reaction between hydrogen and oxygen is formed in the cathode, as described in Eq. (1.5). The total reaction the same as O-SOFC, shown in Eq. (1.3). An overall scheme of the two different configuration is shown in figure 1.2 [13].

$$H_2 \longrightarrow 2H^+ + 2e^- \tag{1.4}$$

$$\frac{1}{2}O_2 + 2H^+ + 2e^- \longrightarrow H_2O \tag{1.5}$$

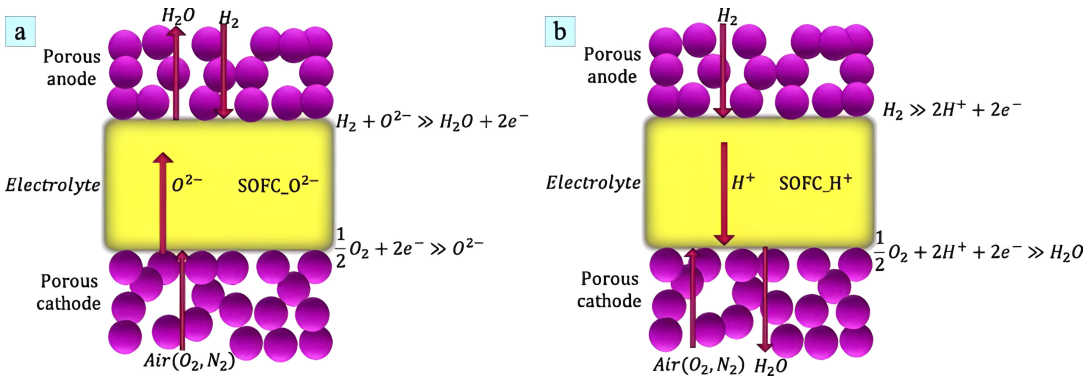


**Figure 1.2:** Schematic of reaction in a) O-SOFC and b) H-SOFC [13].

Ni et al. compared the performance of an ammonia fueled SOFC based on different types of electrolyte. It has been demonstrated that a higher efficiency can be reached for H-SOFC under typical operating conditions due to the high hydrogen partial pressure and low steam partial pressure. Nevertheless, the developing of materials for electrolyte and cathode is important in order to reach high efficiency [14].

## 1.4 Use of SOFC in maritime transporting

The reduction of emission is one of the main goal in the future of the next decade. The ship transport sector is responsible of large amount of emission such as $CO_2$, $NO_x$, VOC and PM [15]. With the aim of a reduction of pollutant and greenhouse gas, the replacement of the Internal Combustion Engine (ICE) with a SOFC is one

of the most promising solution. Furthermore, the electricity that is produced by the SOFC can be used not only for propulsion but also for auxiliaries [16].

Another promising solution is the utilization of a Proton Exchange Membrane Fuel Cells (PEMFC). These cells are characterized by their low working temperature and favorable performances under dynamic working conditions when compared to SOFC. The overall efficiency reaches an average of 40% with a peak of 70% when fueled with pure hydrogen, while SOFC has an average of 60% [16]. An important drawback of PEMFC is the low flexibility in terms of fuel, due to the high required purity of hydrogen, which is hard to store, especially for long distances [17].

The high load variability in ships, because of thermal management related problems, is a crucial challenge in the usage of SOFC. Even if the cell can manage those conditions, as in PEMFC, it is always necessary to pair it with a buffer to reduce its degradation. Between the different approaches that can be adopted to make the SOFC work in a stable condition, there are batteries, supercapacitors and flywheels [16].

De Lorenzo et al. [15] analysed a solution that consists in the usage of batteries in order to avoid dynamic operations of the SOFC. The proposed system uses the electrical energy stored for propulsion, auxiliaries and cooling and the thermal energy produced by the cell for heating purposes. This approach results in an overall energy savings of 12%, due to the high efficiency of the cell. Furthermore, the usage of SOFC alone leads to a significant reduction of local $CO_2$ emissions by 42.23% , while can increase up to 95.5% if the usage of bio-methane is considered.

# Chapter 2

# Thermal management in SOFC

Because the SOFC operates at high temperatures, thermal management of the stack is necessary, especially under dynamic working conditions. The heat produced by the electrochemical reactions can lead to different temperature gradient and to a numerous local hot spot, which can cause non-uniform thermal stress and electrode sintering. A fast start-up process during thermal cycling could also cause structural failures or gas leakages [9].

In figure 2.1 is represented a schematic of the heat transfer inside a planar SOFC. It is possible to observe that all the three mechanism of heat transfer are involved: conduction between the cathode, anode and electrolyte, and convection and radiation through both fuel and air. Is important to mention that the non-uniform electrochemical reaction lead to a different heat generation and heat transfer characteristics among the length of the cell [9].

With respect to radiative exchange, there is a debate about considering it an important actor in heat exchange inside the cell. A study shows by a 2d simulation that radiation is responsible for 70% of the total heat exchange, since radiative heat exchange allows to improve the temperature distribution and reduce the local maximum temperature [18]. Murthy et al. [19] show that the predictive model without considering radiation can overestimate the cell temperature of 180°C if

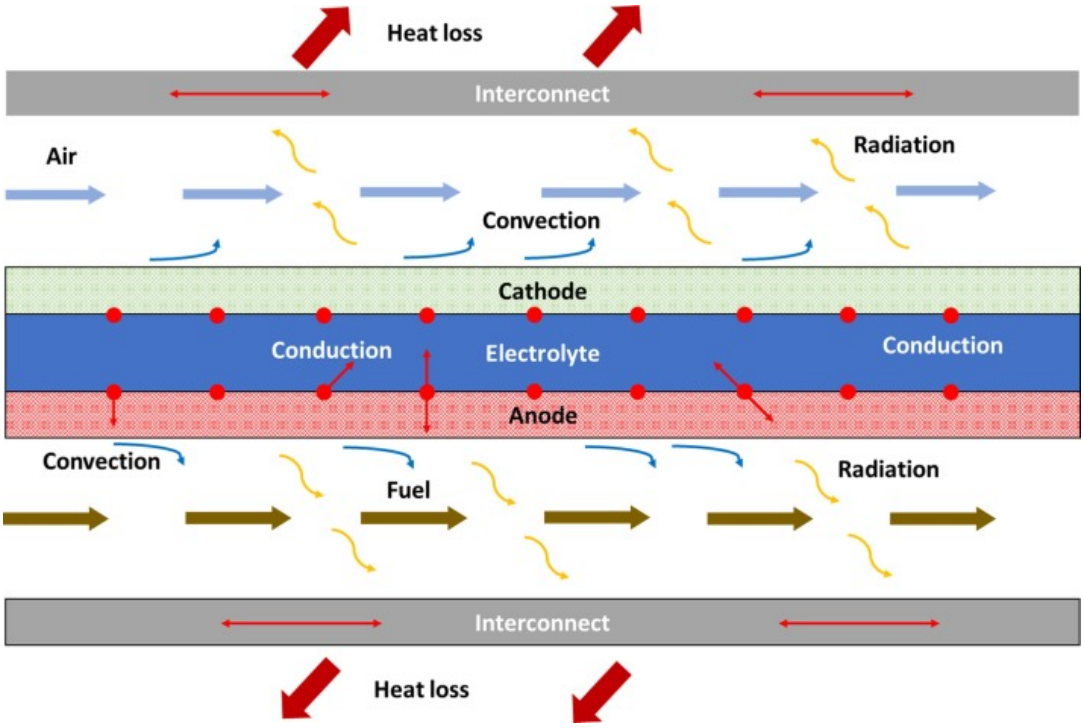


**Figure 2.1:** Schematic of three heat transfer mechanisms in a planar SOFC [9].

compared to a prediction that considers radiation.

However, other studies highlight that radiation can be neglected due to its low contribution to total heat transfer. Damm et al. [20] observed that the difference between a the prediction of a model without considering the radiative effect had a difference of 1°C with respect to experimental measurements. Other studies confirm negligible evidence for the radiative effect [21, 22].

Overall, it is possible to state that the radiative effect can be neglected only if a very precise prediction is required. Considering that if it is taken into account, particular attention must be paid to the choice of the radiative model since the final result is strongly dependent on it [9].

## 2.1 Materials with specific features

Between the different materials used in SOFC, the state of the art favors the use of specific compositions: Yttria Stabilized Zirconia (YSZ) as the electrolyte, Strontium doped Lanthanum Manganite (LSM) as the cathode and Ni/YSZ cermets as the anode. However, thermal cycling conditions can lead to partial detachment at the cathode/electrolyte interface, causing an increase in resistance. In addition, the performance of the cathode can be increased by increasing the number of active reaction sites. One approach consists of using a LSM/YSZ composite electrode with the drawback of an arbitrary distribution of LSM and YSZ particles. Consequently, not all cathode volumes effectively contribute to oxygen reduction reactions [23, 24, 25].

Ni-YSZ cermet are known for the high performances when operating with clean hydrogen and reformed fuels. However, nickel metals are susceptible to reoxidation, deactivation, and oxidation due to fuel contamination, such as sulfur and carbon accumulation (cocking). In order to overcome these drawback, many alternatives for anode material without nickel has been tested. However, despite the good results obtained, their limited compatibility with YSZ electrolyte acts as a significant limitation. With respect to the cathode, LSM-based composites are widely used for SOFC development. However, the utilization of alternative materials is uncommon owing to their unverified long-term stability and restricted compatibility with the electrolyte or other cell components, particularly under the high temperatures that necessary for the fabrication of the cell [24]. Moreover, for H-SOFC, the cathode material can be a limit to the performance. Other alternatives to YSZ for the electrolyte are cerium dioxide-based materials doped with Gadolinium Oxide (GDC), and Lanthanum Gallate-based Materials (LSGM) [25].

## 2.2 Thermal response of the cell/stack to a load variation/cycle

Lin et al. [26] investigated the thermal response of a SOFC stack of multiple cells using a 3D model using finite element analysis. The purpose of the study was to understand the thermal response of the Positive-Electrolyte-Negative Electrode Assembly (PEN) and the gas seals, which can possibly fail. Therefore, gas leaks can lead to cell degradation. Initially, the steady state was calculated by combining electrochemical reactions and heat transfer. The results obtained then were used to calculate the internal stresses. The analysis investigated the effect of the thermal gradients and the Thermal Expansion Coefficient (CTE) of the different materials that compose the stack. In particular, the different CTEs can be shown in figure 2.2.

The study shows that the effect of CTE mismatching produced a greater impact on the distribution of thermal stress compared to temperature gradients alone. In fact, by reducing the CTE mismatching it was possible to observe that the stresses were consequently reduced. Furthermore, the metallic frame were producing the highest effect on the total stress than the glass-ceramic sealant, probably because it is predominant in the total material that compose the cell. For that reason, the development of the frame material with a thermal expansion behavior closer to that of the PEN would lead to a reduction in total stress [26].

## 2.3 Degradation of SOFC's components

The different mechanisms of cell degradation are as follows: cell delamination, cracking, and reaction between components. If a hydrocarbon is used, sulfur poisoning can occur, potentially leading to anode failure due to carbon deposition. Furthermore, Cr poisoning can also occur due to Cr interconnects. A study conducted by

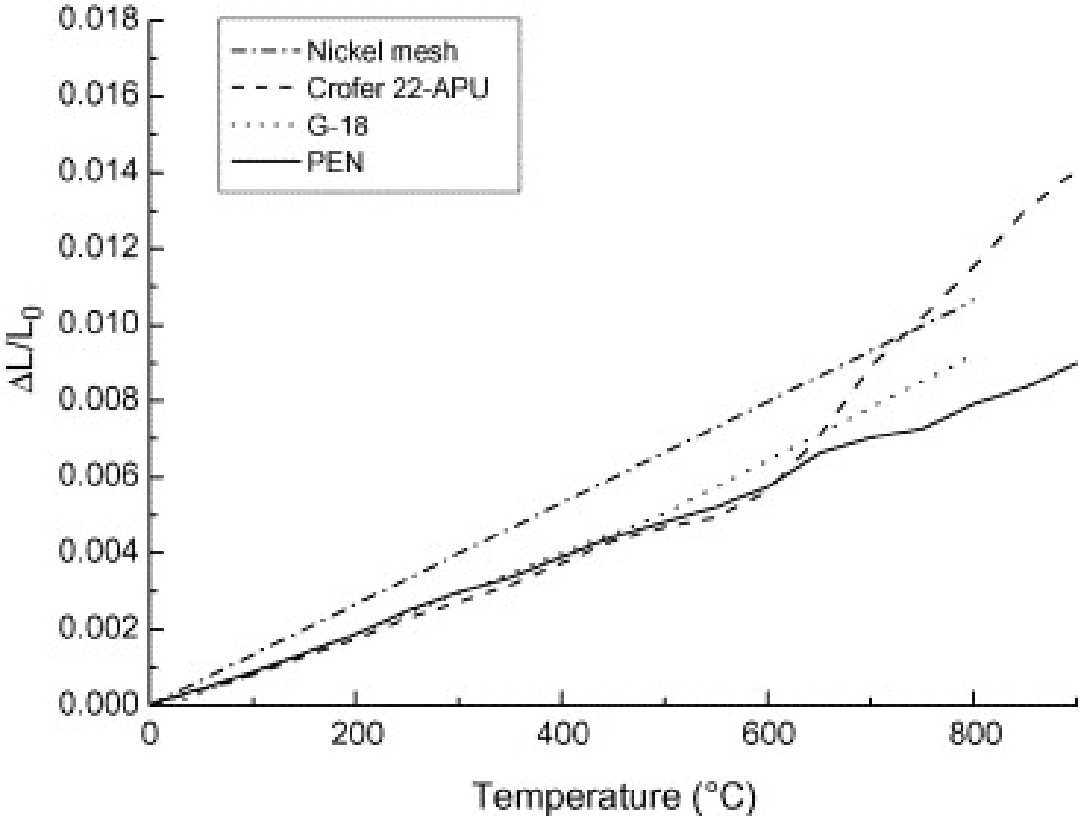


**Figure 2.2:** Thermal expansion behavior of planar SOFC components. The anode supported PEN is composed of Ni/YSZ cermet structure, Crofer 22-APU has been used for frame and interconnects, G-18 (a barium–calcium aluminosilicate glass-ceramic material) for the gas seals and Nickel for the mesh [26]

Park et al. [27] found a reduction in power density and voltage after a 1000h half-cell test. Through SEM analysis, the presence of crack and delamination closed to the cathode-electrolyte interface was identified. A numerical analysis shows that the delamination between the cathode and electrolyte is the major factor contributing to long-term degradation. This effect is more pronounced at high current levels, as it affect the ohmic resistance of the cell. Moreover, delamination reduces the active area, leading to increased oxygen reduction reactions in the remaining intact area to maintain the same current output as before. A schematic of delamination and cracking is represented in figure 2.3.

Cracking and delamination are not only the most common irreversible modes of

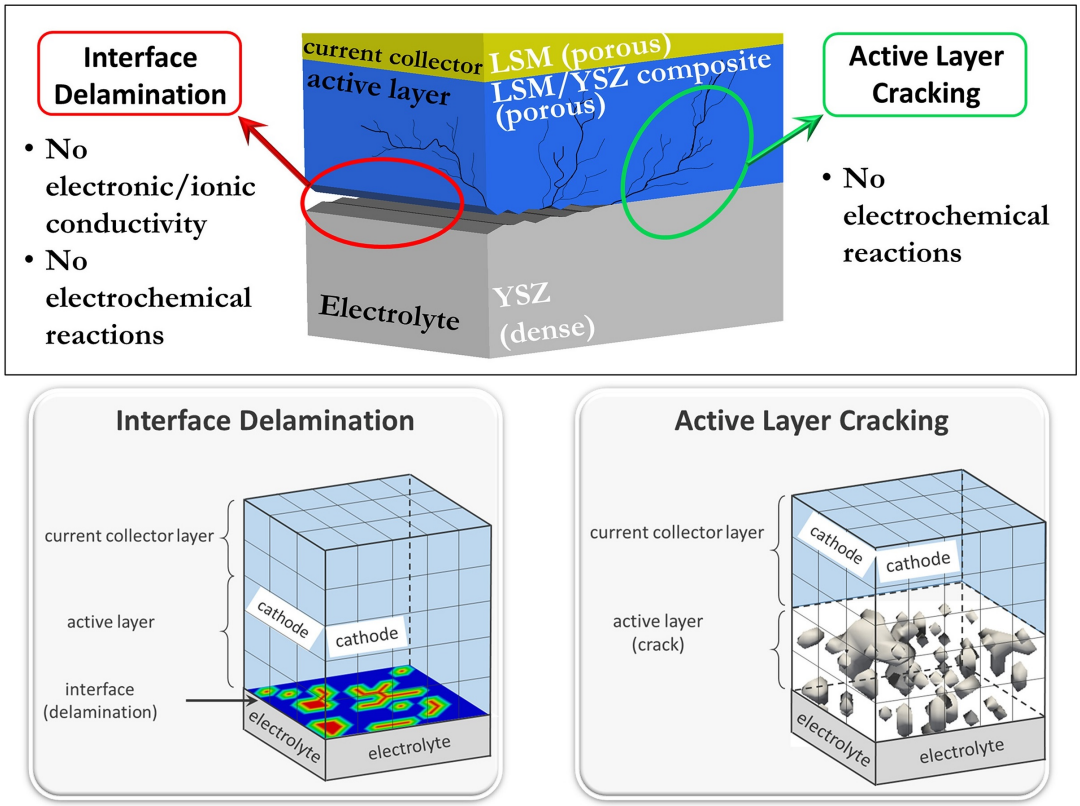


**Figure 2.3:** Schematic of delamination and cracking [28].

degradation of cell performance, but also accelerate other degradation mechanisms. However, their mechanism of formation are still unknowns, and only some models have proposed some explanation. CTE mismatching and localized high-pressure zones can be causes of these phenomena. Furthermore, other degradation mechanism can induce cracks and delamination. A study conducted by Yang et al. [28] analyzed the effects of degradation and cracking using a multi-physics model that considers all the basic physical and electrochemical processes. Initially, the two mechanism were studied separately. However, it is has been demonstrated that the combined effect of both closely resembles the cases analyzed separately.

Delamination affects both ohmic and polarization resistance. This is due to the layer of air formed by the delamination, resulting in the separation of cathode and electrolyte. This layer blocks both electrical conduction and electrochemical

reactions. Instead, cracking within the active layer of the anode influences only the polarization resistance since the electronic and ionic conduction remain intact. The increase in the polarization resistance is due to a loss of reaction sites, essential for the electrochemical reactions. Therefore, the impact of cracking on cell degradation has less influence than that of delamination [28].

## 2.4 Potential solutions

Zeng et al. [9] proposed different solutions aimed at reducing thermal gradients within the cell and, consequently, reducing the stresses induced by the thermal response of the cell. Since the chemical reaction and thermal gradient are affected by the geometry of the gas channels, optimization is possible. Rectangular channels have been shown to effectively reduce thermal gradients. Additionally, it can be also reduced by adopting an inlet design that ensures uniform gas distribution inside the stack. To achieve this, radial guides are used to reduce the temperature of 100°C. Furthermore, the introduction of Ni-mesh helps to reduce local hot spots and thermal gradient, resulting in an increase of 14. 6% in power density. Furthermore, the usage of porous pipes allows to reduce the cell temperature gradient by about 40% and the maximum temperature of 20°C. Furthermore, the co-flow structure is predominantly employed in planar SOFC stacks as it effectively reduces thermal gradients compared to the cross-flow or counter-flow arrangement.

Other possible alternative consists of acting on the working operating conditions of the SOFC. As discussed previously, De Lorenzo et al. [15] examined a solution involving the utilization of batteries to avoid dynamic operations of the SOFC. The proposed system harnesses stored electrical energy for propulsion, auxiliary functions, and cooling, while utilizing the thermal energy generated by the cell for heating purposes..

Promsen et al. [29] presented a novel concept that sees an integration between

Phase-Change Material (PCM) and SOFC. The purpose of that integration is to improve the flexibility of the SOFC in dynamic working conditions, including drastic load variation such as rapid ramp-up and shutdown.

# Chapter 3

# Thermal buffer with PCM

## 3.1 Introduction to latent TES

In addition to Sensible Thermal Energy Storage (STES) and thermochemical energy storage, Latent Thermal Energy Storage (LTES) utilizes PCMs to store heat by exploiting the phase change of a material. LTES are particularly interesting due to the higher energy density it offers compared to STES, as well as its characteristic of exchanging heat at steady-state temperatures [30].

Latent TES shows application in to different fields. In fact, LTES can be used to improve thermal performances of buildings as the PCM can melt during the day and solidify during the night. Consequently, they can prevent overheating during daytime in summer and reduce the thermal cooling need during winter [31].

LTES can also be used for Battery Thermal Management (BTM) in electric vehicles in combination with other cooling techniques [32], since the performance of a battery is strongly affected by temperature. The advantages of low operating cost and good temperature uniformity make latent TES suitable for BTM [33].

Moreover, LTES find application in concentrated solar power plants since they show high potential in efficiency, and economy. In particular, it is possible to implement the latest TES to face the fluctuation of solar power, by storing solar heat when

it is available and releasing it when it is demanded [34]. Furthermore, PCM are also used in electronics, textile industry, and heating, ventilation, and air conditioning [30].

## 3.2 Heat storage with PCM

The type of transformation determines the type of PCM. In particular, can be categorized in to solid-solid, solid-liquid, solid-gas and liquid-gas. Nevertheless, solid-sold phase transformation are usually avoided due to the low latent heat value and the material that include gas in phase change are usually avoided due to large storage volume. In figure 3.1 the categories of PCMs with their advantages and disadvantages is shown [35].

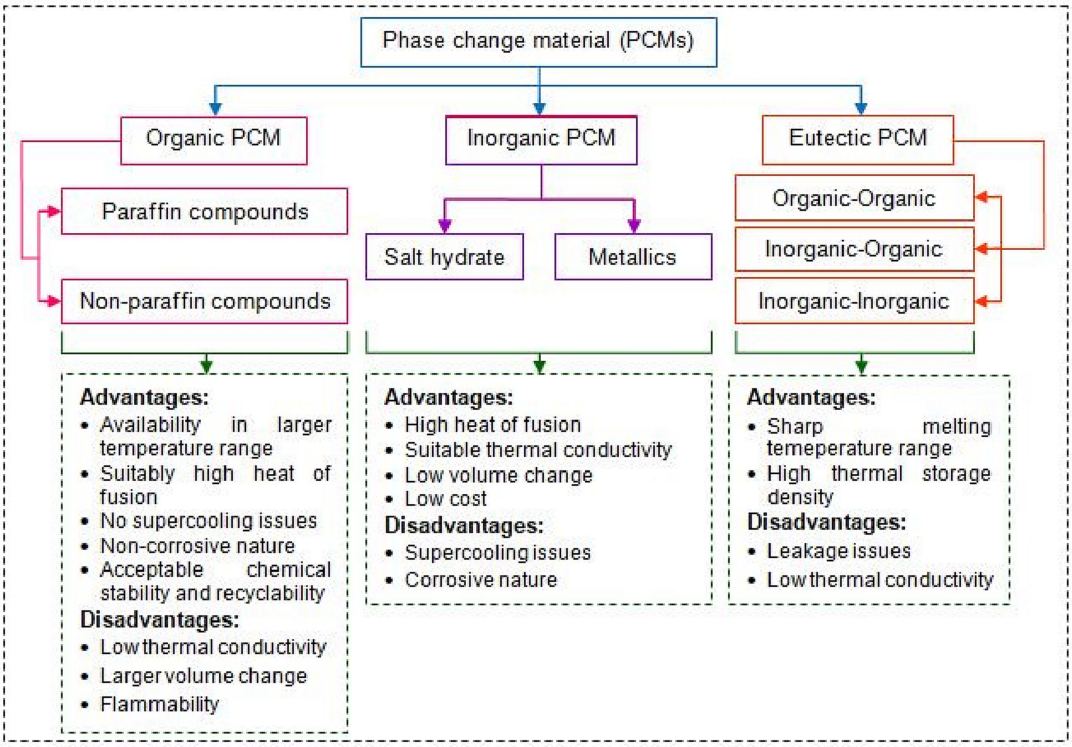


**Figure 3.1:** Classification of PCM [35].

There are many factors that affect the choice of the PCM for each specific ap-

plication. Thermal and physical properties have to be taken into account to ensure that the material absorbs and emits the right amount of energy and has reduced degradation over multiple cycles. Chemical stability has to be especially good when it is in contact with other materials. Furthermore, the kinetics of the transition is a relevant aspect since a fast phase change ensures good heat transfer. Moreover, it is important to avoid hysteresis and supercooling or superheating to make the transition happen without giving additional energy input [30].

## 3.3 Application to the SOFC system

### 3.3.1 Already proposed solutions

According to the publication date of this work, the only proposed SOFC solution that integrates a metallic PCM material is that of Premosent et al. [29]. The study analyzed the thermal response of a standard SOFC stack during partial load, shut-down, and sudden load change by comparing it with a SOFC that integrates a PCM. The material used for PCM is metallic, given the low conductivity of conventional PCMs such as paraffin and hydrated salt. In fact, the high conductivity of a metal allows for good charging and discharging characteristics. The purpose of the PCM is not only to prevent drastic temperature changes, but also to serve as a preheater for both fuel and air inlet.

The 3D model has been used for the study in CFD software to simulate the 24-hour behavior of a two-channel SOFC cell, coupled with a metallic PCM layer. The choice of the materials of the cell has been chosen by analysing the literature and the predicted IV curve is compered with another study. Pure aluminum and an eutectic alloy have been analyzed as a mPCM.

The results show a fast preheating of the inlet gasses that permits to remove the inlet heat exchanger and consequently to exploit all the high enthalpy level of the exhaust gasses in the bottoming system. Moreover, the inlet gases at ambient tem-

perature permit to improve the cooling effect and consequently reach higher current density and power. The simulations also show a uniform temperature distribution of the cell in steady-state conditions, with a temperature difference of 6K. Furthermore, a higher value of air utilization (up to 85%) can be reached, which allows reducing the parasitic losses of a standard SOFC operation.

During the shutdown phase, it has been observed that the temperature decrease is drastically reduced after the introduction of the PCM into the cell. In addition, during extreme load variation, the mPCM-SOFC show a temperature decrease of 100K for the aluminum and 40K for the alloy. This difference can be reduced by choosing an operating cell temperature that is closer to the melting temperature of the PCM. The ability of the mPCM-SOFC to operate under dynamic conditions allows it to be coupled with renewable energy sources that have intrinsic variability and adopt it for maritime operations.

### 3.3.2 Candidate materials

For the reasons explained above, good PCM candidates are metallic PCM (mPCM). Single-component materials as well as eutectic mixtures (EPCM) can be used. EPCMs are characterized by having a melting point that is affected by their composition. Therefore, they can be synthesized in order to adapt the melting point to the specific application. Moreover, the high thermal conductivity, low degree of supercooling, and reduced vapor pressure make them interesting candidates. Regarding the cost and availability of materials, magnesium, zinc, silicon, and aluminum were identified as the most suitable options due to their price ranges (approximately between 2-3 $/kg), and their extensive use [36].

The mPCM used in the stack should have a melting point that is close to the operating point of the stack to reduce the temperature decrease after a load reduction [29]. In table 3.1 is represented a list of mPCMs with melting point characteristics that can fit a SOFC stack that has an operating temperature in the range of 700°C

and 750°C.

Mixture of Cu-Si and Cu-Mg can be used for that application as the melting point is in the operative rage of the stack. As mentioned above, the combination of the materials affects the melting point. For that reason, a percentage in the range of 100-90% or 70-0% Cu for the Cu-Si mixture and 100-95% for the Cu-Mg. Moreover, Cu has a melting temperature of 811°C, Mg of 376°C and Si of 1127°C [40].

In contrast, Zn and Mg alloys cannot be used for a stack operating at 700-750°C, since the melting point is lower than 650°C. Therefore, the phase change cannot be exploited during a load reduction of the stack [41].

### 3.3.3 Containment material

The encapsulation of PCMs materials is a technology that allows the use of PCMs to be extended in practical applications by preventing leakages during the phase change of the material. Encapsulated PCMs can be classified according to their dimensions into Nano-EPCMs (less than $1\mu m$), Micro-EPCMs ($1\mu m - 1mm$) and Macro-EPCMs (more than $1mm$) [42]. The choice of containment material for PCM encapsulation has a high dependency on the application. The choice between metallic, ceramic and polymeric shells depend on the property of the material and will affect the mechanic and thermal characteristics of the capsules. In figure 3.2 are shown the main characteristics of containment materials [43].

Alumina ($Al_2O_3$) is a widely recognized ceramic, frequently employed as an inert crucible in both laboratory and industrial settings. Their ability to undergo elastic deformation makes them suitable for numerous applications, despite their drawbacks of brittleness, machinability, and cost. Iron can be also used for eutectic materials that involves magnesium, as it exhibits no significant solubility with both liquid and solid phase magnesium. Graphite is also appealing as a possible containment material due to its affordability. However, limitations in the assessed CALPHAD systems have restricted its compatibility to only pure mPCMs at equilibrium. Fur-

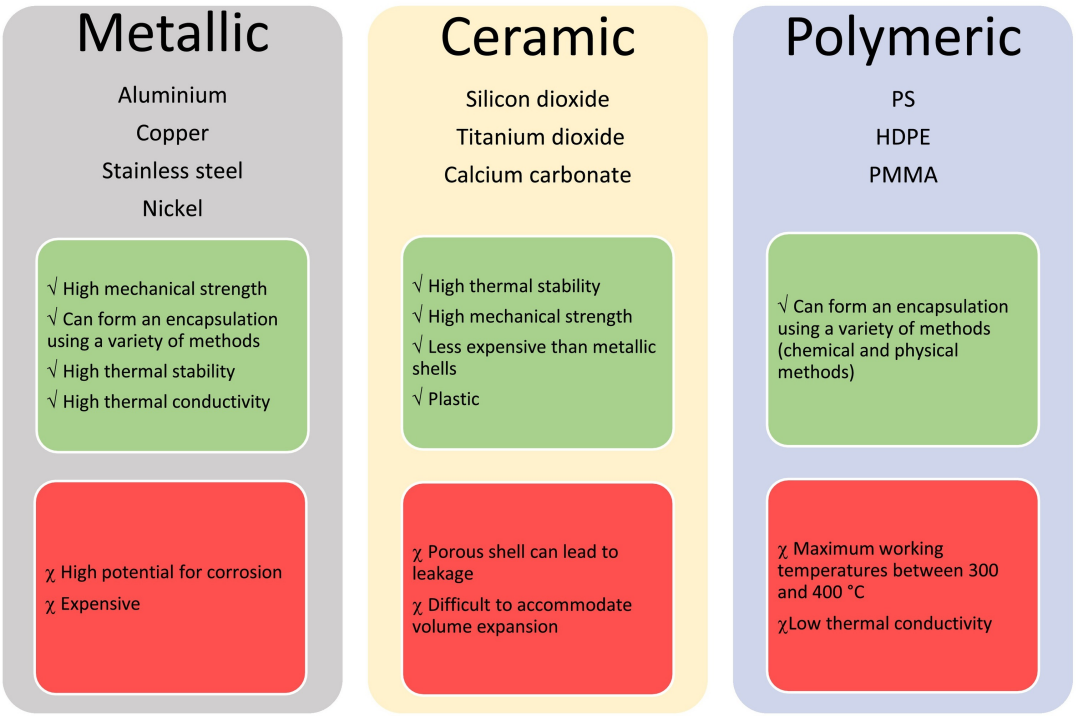


**Figure 3.2:** Classification and characteristics of PCM shell materials [43].

thermore, magnesia ($MgO$) seems a promising container for mPCMs that contains magnesium despite its brittleness and high relative cost [37].

### Encapsulation related problems

The encapsulation of high temperature metallic PCM can pose some challenge due to the corrosion of the metallic shells. Therefore, ceramic containers are a promising solution due to their high corrosion resistance and good thermal conductivity. Moreover, the expansion of the PCM during the phase transition can lead to cracks in the shell material, especially for high temperature PCMs. For this reason, encapsulation at room temperature may not be preferred. Therefore, the volume expansion is a factor that must be taken in to account in the encapsulation process [42, 44].

The study proposed by Scheng et al. [42] introduces a novel macro-encapsulation strategy that uses $Al_2O_3$ to manufacture $Cu@Al_2O_2$ capsules, which contain gaps between the shells and the cores. The spherical capsules are sintered in two phases,

one at low temperature and the other at high temperature. The high-temperature phase is carried out in a furnace under protective argon, with carbon powder used to prevent oxidation since it can react with the residual oxygen. The results of the study demonstrate that this technique can produce macro-capsule with excellent cyclic durability and high heat storage capability.

The macro-encapsulation mechanism proposed by Fukatori et al. [44] concerns a container composed of a cup and a cap sealed together by a film of Al that is bolted around a part of the cup. During heating, the melting phase of the PCM leads to stresses that lift the cap due to the expansion of the material. When the temperature reaches the melting point ($T_{melt}$) of Al, it melts and seals the cup and cap to encapsulate the PCM. After cooling, since the void in the capsule is at low pressure, it can act as a buffer space during the phase change of the material. The container showed an excellent cyclic durability after a 100 cycle test, demonstrating a uniform temperature trend over all the cycles. Moreover, the proposed capsule can prevent corrosion of the liquid metal.

| **Compound** $[weight\%]$ | **Melting point** $[°C]$ | **Density** $[kg.m^{-3}]$ | **Heat capacity** $[J.kg^{-1}K^{-1}]$ | **Enthalpy of melting** $[kJ.kg^{-1}]$ | **Ref.** |
|---|---|---|---|---|---|
| $Cu_{57.2}Mg_{5.5}Mg_{37.3}$ | 700 | 6889 | 540 | 151 | [37] |
| $Zn_{49}Cu_{45}Mg_6$ | 703 | 8670 | 420 | 176 | [38] |
| $Cu_{72.5}Mg_{11.4}Mn_{16.1}$ | 709 | 6165 | 640 | 246 | [37] |
| $Cu_{91}Zn_9$ | 715 | 5600 | - | 134 | [39] |
| $Cu_{69}Zn_{17}P_{14}$ | 720 | 7000 | 540 | 368 | [39] |
| $Cu_{90.8}Mg_{9.2}$ | 726 | 6484 | 530 | 200 | [37] |
| $Cu_{65.5}Ni_1Sn_{33.5}$ | 744 | 8056 | 660 | 146 | [37] |
| $Cu_{74}Zn_{19}Si_7$ | 765 | 7170 | - | 125 | [36, 38] |
| $Cu_{56}Si_{27}Mg_{17}$ | 770 | 4150 | 750 | 420 | [29, 36, 38] |
| $Mg_{84}Ca_{16}$ | 790 | 1380 | - | 272 | [39] |
| $Mg_{47}Si_{38}Zn_{15}$ | 800 | - | - | 314 | [39] |
| $Cu_{80}Si_{20}$ | 803 | 6600 | 500 | 197 | [36, 38] |
| $Cu_{83.6}Si_{16.4}$ | 803 | 5830 | 510 | 231 | [37] |
| $Al_{12.2}CU_{79.9}Mg_{7.9}$ | 812 | 6107 | 540 | 188 | [37] |
| $Cu_{90.5}Si_{9.5}$ | 820 | 6196 | 490 | 100 | [37] |
| $Cu_{40.3}Zn_{59.7}$ | 836 | 7836 | 450 | 170 | [37] |
| $Cu_{83}P_{10}Si_7$ | 840 | 6880 | - | 243 | [39] |
| $Mg_2CU$ | 841 | - | - | 243 | [38] |
| $Cr_{1.1}Cu_{63.9}Mn_{35.0}$ | 864 | 7839 | 640 | 150 | [37] |
| $Si_{49}Mg_{30}Ca_{21}$ | 865 | 2250 | - | 305 | [39, 38] |
| $Al_{45}Si_{40}Fe_{15}$ | 869 | 3360 | 810 | 562 | [38] |
| $Ni_{27.8}Zn_{72.2}$ | 881 | 7506 | 490 | 271 | [37] |
| $Cu_{58.6}Fe_{1.2}Zn_{40.1}$ | 900 | 8252 | 700 | 154 | [37] |

***Table 3.1:*** *Metallic PCMs properties.*

# Chapter 4

# SOFC stack modeling

## 4.1 Introduction to SOFC modeling

A study led by Yoon et al. [45] investigated anode-supported SOFCs fabricated using a single-step cofiring process. In this study, experimentally measured I-V (current-voltage) curve were fitted to the polarization model of the cell, and other cell parameters were obtained at different temperature conditions. Moreover, the polarization resistances calculated by the model were verified by impedance spectroscopy, showing good agreement. Another study by Wang et al. [46] provided experimental validation of the SOFC polarization model. The experimental results show a close match with the model calculation, enhancing confidence in the use of polarization modeling to evaluate SOFC performance.

Gebregergis et al. [47] discussed the modeling of an SOFC using distributed and lumped modeling approaches. The two approached were then compared with the experimental results. The fundamental relations describing the operation of a cell were kept the same for both approaches. While in the distributed model, the partial pressures are assumed to be dependent from the length of the cell, in the lumped model they are calculated by an equivalent RC circuit. Steady state conditions showed agreement between the experimental set-up, the lumped model

and the distributed model. Moreover, the dynamic behavior described by the two models exhibited similar time responses, and the predicted cell voltage was similar to that of an actual fuel cell. It was also observed that the time response of the cell did not strongly depend on the temperature.

Padulles et al. [48] developed an SOFC model that considers species dynamics for a fuel cell-based power plant. The dynamics of the model were expressed in the Laplace transform domain. A power conditioning unit was developed to handle load changes because rapid changes in current could damage the stack. However, the model did not consider temperature dynamics.

Sedghisigarchi and Feliachi [49] developed a detailed dynamic model of a SOFC for small signal and transient stability studies. The model comprised an electrochemical model and a thermal model, taking into account the Nernst voltage equation and all polarization losses in the calculation of the output voltage. The model demonstrated that species and temperature dynamics play an important role in slow transients, while confirming that they can be neglected in fast transients. Furthermore, standalone simulations were initially conducted, and after a power analysis toolbox (PAT) in MATLAB was developed to simulate a power system containing a fuel cell.

Hall and Colclaser [50] proposed a model that simulates the transient operation of a tubular SOFC in response to changes in electrical load. The model contains an eletrochemical and a thermal parts that are verified separately before were combined in to the transient model. Moreover, the steady-state conditions can also be determined by running the transient simulations Until the transients decay to a level specified amount. The cell was subjected to a step increase in current density while keeping all input gas flows constant. The results showed a behavior similar to that of a planar SOFC in a previously published study.

The study by Achenbach [51] theoretically addressed the change of load of an SOFC stack. The transient was introduced by changing the current provided by the

cell with a step increase. The results revealed an undershoot of the voltage during the intermediate period, which after a relaxation time increased to a steady-state value. The undershoot is attributed to the temperature of the cell, which just after the step increase of current remains low. Then, the temperature starts to increase because of the higher heat produced and consequently the voltage increase. The study also demonstrated that the temporal variation of the cell voltage depends on the temperature and that the relaxation time is correlated with the cell design parameters. A longer response time can also be observed when the step increase in current is low. Moreover, it has been shown that the relaxation time remains the same for a step increase or decrease of the current.

Barelli et al. [52] developed a dynamic SOFC model that work in load following operation with the aim of maintaining the temperature constant, done by adjusting the cathodic air flow. An experimental campaign was carried out in which the temperature of the cell was evaluated as a mean of two temperature measurements at the interconnection between two central cells. In this campaign, the air flow variation was imposed in terms of oxidant utilization ($U_{ox}$). The results showed that a decrease in oxidant utilization was leading to a decrease in temperature, especially at low temperatures. The thermal section has been developed by considering the enthalpy in the inlet and outlet flow rates and thermal losses that follows a trend line depending on the electric load. The energy balance considered was based on a study conduced by Yang et al. [53], where a modified Takagi-Sugeno fuzzy model was developed.

## 4.2 SOFC dynamic model

### 4.2.1 Electrochemical model

The polarization model of an SOFC consists in determining the I-V curve of the cell, which can be useful to comprehend the behavior of the cell/stack. The voltage

across a single cell $V_c$ is given by equation 4.1.

$$V_c = E_{ocv} - V_{act} - V_{ohm} - V_{conc} \tag{4.1}$$

Where $E_t$ is the Nernst reversible voltage (also called the opec circuit voltage), $V_{act}$ are the activation loss, $V_{ohm}$ are the ohmic loss, and $V_{conc}$ are the concentration loss [47, 49, 48]. All losses are generated at the moment in which the cell starts to supply current to a load. In this condition, a voltage due to internal charge transfer, conduction, and diffusion processes is generated. Moreover, the polarization losses are then taken into account by three terms. The activation losses are associated with the reaction energy barrier at the electrode-electrolyte interfaces. The ohmic losses account for the passage of electrons in the interconnects and electrodes and the passage of ions in the electrolyte. Concentration losses represent the limited diffusion of reactant and product from the bulk flow to the reaction sites [54].

**Nernst reversible voltage**

The Nernst potential is the reversible voltage that can be measured across the cell under open circuit (OC) conditions. In fact, when the SOFC is not connected to an external load and then no current is flowing in the cell, it is typically assumed that the voltage is equivalent to the equilibrium Nernst potential. It is given in equation 4.4, and it is constituted by a component under standard conditions (eq. 4.2), a temperature dependent term, and a pressure-dependent term to take into account both the temperature and pressure influence. Furthermore, the component under standard condition can be also grouped with the temperature dependent term, as in eq. 4.3.

$$E^0 = -\frac{\Delta \bar{g}_r^0}{nF} \tag{4.2}$$

$$E^{0T} = E^0 + \frac{\Delta\bar{s}}{n}(T - T_0) \tag{4.3}$$

$$E_{ocv} = E^{0T} + \frac{RT}{nF} ln \left( \frac{\prod a_r^{\nu_i}}{\prod a_p^{\nu_i}} \right) \tag{4.4}$$

Where $\Delta\bar{g}_r^0$ is the standard-state free-energy change for the reaction, $n$ is the number of moles electrons transferred, $F$ is the Faraday constant, $\Delta\bar{s}$ is the entropy variation, $T$ is the working temperature, $T_0$ is the standard temperature, $R$ is the ideal gas constant, $a_p$ is the activity of products, $a_r$ is the activity of reactants, and $\nu_i$ is the stoichiometric coefficient of the single species [55].

### Activation losses

Activation losses occur as a result of overcoming the energy barriers for the reactions at the interfaces between the electrode and electrolyte. This loss was commonly neglected since its low value reached at 1000°C temperature operation and because of the predominance of ohmic losses. However, the modern stack utilizes planar geometries and operates under 800°C, which poses the need of considering activation losses. The Butler-Volmer (B-V) equation is usually considered as the governing equation for activation losses, as shown in eq. 4.5, where $I_c$ express the current in the cells, and $I_0$ is the exchange current [54].

$$I_c = I_0 \left[ exp\left( \alpha_1 \frac{F}{RT} V_{act} \right) - exp\left( -\alpha_2 \frac{F}{RT} V_{act} \right) \right] \tag{4.5}$$

The coefficients $\alpha_1$ represent the reduction transfer coefficient and $\alpha_2$ the oxidation transfer coefficient. The two coefficients are dependent on the electron transfer process that occurs at the electrode-electrolyte interface. The expression of the activation losses can be derived by B-V equation, resulting in the high-field approximation (also called Tafel equation) valid when $i > 4i_0$, and low-field approximation,

valid for $i < i_0$. However, both of the two approximations do not accurately describe the B-V curve for the whole range of current. Therefore, if it is assumed that $\alpha_1 = \alpha_2$, it is possible to express the activation losses as in equation 4.6. The approximation with the hyperbolic sine results in a well match with the experimental data [47, 54].

$$V_{act} = \frac{RT}{F} sinh^{-1}\left(\frac{I_c}{2I_0}\right) \tag{4.6}$$

The exchange current $I_0$ ca be calculated by the Arrehenius-type relation, as shown in eq. 4.7, where $\psi$ is the pre-exponential factor, $E_{act}$ is the activation energy of the chemical reaction [47].

$$I_0 = \psi \cdot exp\left(-\frac{E_{act}}{RT}\right) \tag{4.7}$$

**Ohmic losses**

The ohmic losses are primarily associated with the passage of ions through the electrolyte. To minimize these losses, it is crucial to use materials with high ionic conductivity and to keep the electrolyte thickness as small as possible. Yttria Stabilized Zirconia (YSZ) is the most commonly used electrolyte material due to its excellent stability in both oxidative and reductive environments. At a thickness of $10\mu m$, YSZ exhibits a resistance of $0.05\Omega cm^2$ at $800°C$. However, it is important to note that activation and concentration losses can often exceed the ohmic contribution, thereby increasing the specific resistance of the cell [56].

The Ohmic losses are given by the equation 4.8 where $\gamma = 0.2\Omega$ and $\beta = -2870K$ are the constant coefficient of the fuel cell, $T_0 = 973K$ is the reference temperature, $r$ is than the internal resistance of the cell [49, 57].

$$V_{ohm} = r \cdot I_c = \gamma \cdot exp\left[\beta\left(\frac{1}{T_0} - \frac{1}{T}\right)\right] \cdot I_c \tag{4.8}$$

### Concentration losses

Concentration losses arise due to diffusion of gases inside the electrodes. In particular, due to anodic transport of $H_2$ and $H_2O$, and due to a cathodic contribution from $O_2$ transport. These two terms depend, respectively, on the anodic and the cathodic saturation current density, which function based on the binary diffusivity of the respective species transported by the anode and cathode [46]. The concentration losses are given by equation 4.9 where $I_L$ is the limiting current of the cell [57].

$$V_{conc} = -\frac{RT}{nf} ln\left(1 - \frac{I_c}{I_L}\right) \tag{4.9}$$

Concentration polarization can be more present when the thickness of the electrode is relatively thick, as in anode-supported fuel cell. Having an anode substrate with good diffusion properties is then necessary to improve the catalytic activity. For that reason, the fabrication of a material with good pore size and high porosity is essential to reach high power densities [58].

### Area Specific Resistance

The losses calculation can also be done by considering an Area Specific Resistance (ASR) that is temperature dependent and summarize the activation, concentration and ohmic losses. By using the ASR the output voltage can be calculates as in equation 4.10.

$$V_c = E_t - ASR(T) \cdot I \tag{4.10}$$

### Calculation of the activity

By considering the hypothesis of ideal gas, the activity of the species can be replaced by the partial pressure ($p_i$) since, for ideal gas $a_i = p_i/p_o$. Therefore, the Nernst potential is given in equation 4.11 by considering the reaction in equation 1.3 [55].

$$E = E_T + \frac{RT}{nF} ln \left( \frac{p_{H_2} p_{O_2}^{0.5}}{p_{H_2O}} \right) \tag{4.11}$$

The partial pressures can be determined using the ideal gas law and by deriving the pressure term by time. Then, using the Laplace transformation, it is possible to obtain equations 4.12, 4.13, 4.14. Where $K_i$ is the molar valve constant $[kmol/(atm \cdot s)]$, $\tau_i$ is the value of the pole $[s]$, $q_i$ is the inlet mass flow $[mol/s]$, and $z_i$ is the charge number, that is 2 for hydrogen and water and 4 for oxygen [48].

$$p_{H_2} = \left( \frac{\frac{1}{K_{H_2}}}{1 + \tau_{H_2} s} \right) \left( \dot{q}_{H_2} - \frac{I_c}{z_{H_2} \cdot F} \right) \tag{4.12}$$

$$p_{O_2} = \left( \frac{\frac{1}{K_{O_2}}}{1 + \tau_{O_2} s} \right) \left( \dot{q}_{O_2} - \frac{I_c}{z_{O_2} \cdot F} \right) \tag{4.13}$$

$$p_{H_2O} = \left( \frac{\frac{1}{K_{H_2O}}}{1 + \tau_{H_2O} s} \right) \left( \frac{I_c}{z_{H_2O} \cdot F} \right) \tag{4.14}$$

The determination of the partial pressure can be done considering an equivalent RC circuit, as suggested by Gebregergis [47]. Its Laplace transforms are given in eq.

4.15 and eq. 4.16 where $K_{=}1/R$, $\tau = RC$, and $C = V/RT$.

$$C\frac{dV_c}{dt} = I_c - \frac{V_c}{R} \tag{4.15}$$

$$V_c(s) = \frac{R}{1 + RC \cdot s} \cdot I_c(s) \tag{4.16}$$

### 4.2.2 Thermal model

Since the behavior of a cell/stack strongly depends on the temperature, it must be accurately determined to evaluate the SOFC performance. As already mentioned in Section 2, a change in load will also affect the heat generated inside the cell/stack and, therefore, its temperature. In particular, the heat generated by a single cell is given in equation 4.17 [55].

$$\phi_{cell} = \left(-\frac{\Delta\bar{h}}{zF} - V_c\right) \cdot I_c \tag{4.17}$$

Moreover, in eq. 4.18, the energy balance of a SOFC stack is expressed, where $M_c$ is the mass of the cell, $c_p$ is the heat capacity of the cell/stack unit, and $\Sigma Q_i$ represents the sum of all the heat transferred and source terms. Using this energy balance, it is possible to determine the temperature dynamic.

$$M_c \cdot c_p \cdot \frac{dT}{dt} = \sum Q_i = \frac{dH}{dt} \tag{4.18}$$

As suggested by Hall et Colclaser [50] the balance can be solved by applying the Euler method. In this way, by knowing the initial temperature value, it is possible to determine its variation as in eq. 4.19, where the temperature is calculated for

each instant, based on its value the instant before. The derivative of enthalpy can be calculated as in equation 4.20.

$$T_k = T_{k-1} + \Delta t \cdot \frac{\Delta H}{M_c \dot{c}_p} \tag{4.19}$$

$$Q_{net} = \Delta H = \frac{dH}{dt} = \dot{H}_{in} - \dot{H}_{out} - P_{out} - \phi_{loss} \tag{4.20}$$

Furthermore, it is assumed that the stack feeding gas is composed of: 66. 6% of $H_2$, 13. 2% of $CO$, 6. 8% of $CO_2$ and 13.2% of $H_2O$. For that reason, the enthalpy flows (input and output) were calculated by considering not only oxygen and hydrogen but also all of the chemical species that compose the feeding gas, as shown in eq. 4.21. The enthalpies of each spice are calculated in Python by using a library called "PYroMat". Moreover, it is important to say that it is considered that only $H_2$ is generating current.

$$H = \dot{q}_{H_2} h_{H_2} + \dot{q}_{CO} h_{CO} + \dot{q}_{H_2O} h_{H_2O} + \dot{q}_{CO_2} h_{CO_2} + \dot{q}_{N_2} h_{N_2} + \dot{q}_{O_2} h_{O_2} \tag{4.21}$$

It is considered for both inlet air and hydrogen, that only a portion will be used for power generation. For this reason, the fuel utilization (eq. 4.22) and the oxidant utilization (eq. 4.23) are used to determine the generated current.

$$U_f = \frac{I \cdot N_0}{z_{H_2} F \cdot \dot{q_{H_2}}} \tag{4.22}$$

$$U_{ox} = \frac{I \cdot N_0}{z_{O_2} F \cdot \dot{q_{O_2}}} \tag{4.23}$$

The loss factor (eq. 4.24) is taken from a study conducted by Barelli et al. and is expressed as a percentage of the total input energy of the system (where $c_1 = 0.137$; $c_2 = -0.273$; $c_3 = 0.328$). This term is evaluated in the study in an experimental campaign, through a tuning activity done in the study of Barelli et al. [52]. In particular, the loss term is evaluated in function of the total input energy ($H_{loss}$), calculated in equation 4.25, and it is represented in figure 4.1.

$$\phi_{loss} = \left[ c_1 \cdot \left( \frac{P_c}{P_{max}} \right)^2 + c_2 \cdot \frac{P_c}{P_{max}} + c_3 \right] \cdot H_{loss} \tag{4.24}$$

$$H_{loss} = \dot{q}_{H_2,in} h_{H_2} + \dot{q}_{CO,in} h_{CO} + \dot{q}_{N_2,in} h_{N_2} + \dot{q}_{O_2,in} h_{O_2} \tag{4.25}$$

**Implementation of PCM**

The implementation of PCM has been done considering that in case of $\Delta H \simeq 0$, the temperature remains constant and there is no change in the phase of the material. On the contrary, if $\Delta H \neq 0$, depending on the working temperature and on the operating temperature of the PCM, the material can melt or solidify by absorbing or releasing heat and by that, maintaining the temperature constant.

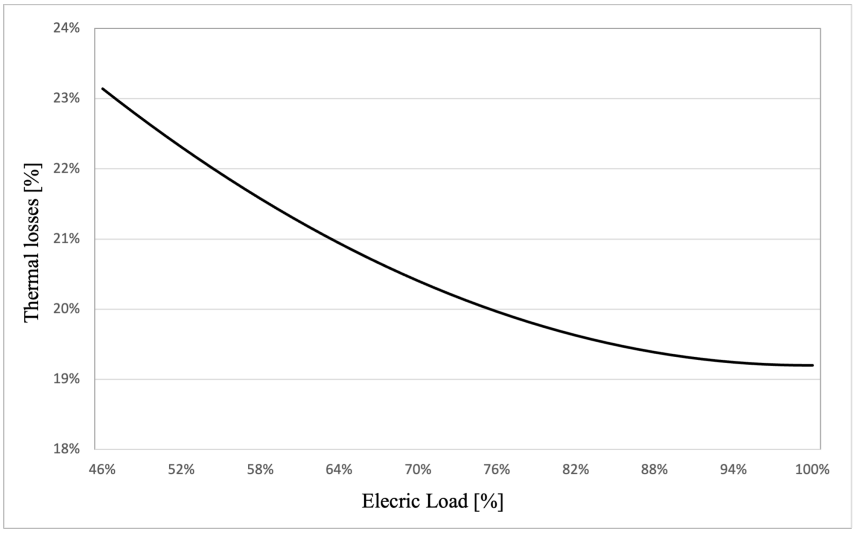


**Figure 4.1:** Thermal losses calculation [52].

## 4.3 Model implementation in Python

The model of the stack that has been implemented by using the equation described in Section 4.2. It has been organized in a file called *"main"* that imports some functions used for the calculation of partial pressure and enthalpy, present in the file *"functions"*. All the constants are stored in an excel file and red by the model before each execution, and after the simulation, all the variables calculated are stored in an another excel file to perform further analysis. Inside the input file is also present the values molar flow rate of $\dot{q}_{H_2,eq}$ in function of time that will define the input step function of the model. Moreover, the simulation will execute for a fixed period of time $t$ and will perform calculations each instant $dt$ defined in the input file.

Moreover, the dynamic model is structured to perform three different type of simulations described in the following list, that can be selected in the input file by changing the parameter "simulation". In this way, just by changing one parameter in the input file, is it possible to switch between the simulation of the polarization curve (simulation 1), the step load curve (simulation 1) and the real case curve

(simulation 2). Simulation 0 and 1 are used for the validation, described in the next section, and simulation 2 is used to scale the stack to the nominal power of 95kW in order to simulate a real input load described in the next chapter. When the model work in simulation 2, there are two scaling parameters that are considered. The first represent the power scale and is called "*power_increase*". The second is called "*time_increase*" and permits to scale the real load input curve to higher times. In this way, it is possible to analyze the influence of the total time of simulation.

1. Simulation 0: Polarization curve;
2. Simulation 1: Step load curve;
3. Simulation 2: Real case curve.

In addition, the dynamic model can work in three different modality, that can be selected in the input file by changing the parameter "mode":

1. Mode 0: The temperature of the stack is maintained constant;
2. Mode 1: The temperature is calculated without considering the PCM;
3. Mode 2: The temperature is calculated implementing the PCM.

### 4.3.1 Electrochemical model

#### Calculation of the partial pressure

The calculation of the partial pressure is done in a function called *"part_press"* that, after reading all the variables required from the excel sheet (*'sheet_in'*) given as an input parameter, it calculates the Laplace function for all three species by calling a function called *"laplace"*. Then, the Laplace function is elaborated in a function called *"pp"* that return the array of time, current, and pressure for each spice. Before returning all the variables, the fuel excess $E_f$ (eq. 4.26) and the oxygen excess $E_{ox}$ (eq. 4.27) are converted in an array with the same length of the time.

$$E_f = 1/U_f \tag{4.26}$$

$$E_{ox} = 1/U_{ox} \tag{4.27}$$

```
def part_press(sheet_in_name, file_path_in):

    if simulation == 2:
            l = l*time_increase

    for k in range(0, steps):
        if simulation == 0:
            t_column, q_h2_i_column, uf_column = 'F', 'G', 'H'
            t_in.append(sheet_input[f'{t_column}{k+3}'].value)
            q_h2_i.append((sheet_input[f'{q_h2_i_column}{k+3}'].value)/(60*vol_std))
            Ef.append(1/(sheet_input[f'{uf_column}{k+3}'].value))
        elif simulation == 1:
            t_column, q_h2_i_column = 'J', 'K'
            t_in.append(sheet_input[f'{t_column}{k+3}'].value)
            q_h2_i.append((sheet_input[f'{q_h2_i_column}{k+3}'].value)/(60*vol_std))
            Ef.append(1/0.75)
        elif simulation == 2:
            t_column, q_h2_i_column = 'M', 'N'
            t_in.append(sheet_input[f'{t_column}{k+3}'].value*time_increase)
            q_h2_i.append((sheet_input[f'{q_h2_i_column}{k+3}'].value)/(60*vol_std))
            Ef.append(1/0.75)

        q_h2o_i.append(q_h2_i[k] * 13.2/(66.8*Ef[k]))
        I.append(q_h2_i[k]*z_h2*F/(N0*Ef[k]))
        Eox.append(1/u_ox)
        q_o2_i.append(q_h2_i[k] * Eox[k]/(2*Ef[k]))

    i_s, u_s_h2 = laplace(q_h2_i, t_in, I, gh2, Kr, DT)
    i_s, u_s_o2 = laplace(q_o2_i, t_in, I, go2, Kr, DT)
    i_s, u_s_h2o = laplace(q_h2o_i, t_in, I, gh2o, Kr, DT)

    time, curr, p_h2 = pp(i_s, u_s_h2, Kh2, Th2, dt, DT, l)
    time, curr, p_o2 = pp(i_s, u_s_o2, Ko2, To2, dt, DT, l)
    time, curr, p_h2o = pp(i_s, u_s_h2o, Kh2o, Th2o, dt, DT, l)

    return time, curr, e_f, e_ox, p_h2, p_o2, p_h2o
```

The for cycle (from zero to *step*) is used to read the input value of time and the equivalent hydrogen molar flow rate given to the stack. The input function will be a step function that will approximate the real trend of a load. Moreover, the current $I\_in$ is calculated by using the hydrogen equivalent flow rate and the fuel utilization. The two functions called inside the cycle (*"laplace"* and *"pp"*) are then described. In addiction, inside the for cycle the read and calculated variables depend also on the type of the simulation.

### Laplace transform

The input Laplace input function $U\_in$ is created in the function *"laplace"*, that will receive as an input the array of mass flow rate $q\_in$, the array of instant of time $t\_in$, the current output of the cell $I\_in$, the parameter $g$, the Faraday constant $F$ and the parameter $DT$.

```
1  def laplace(q_in, t_in, I_in, g, Kr, DT):
2
3      U_in = []
4
5      for k in range(0, len(q_in)):
6          U_in.append(q_in[k] - g*Kr*I_in[k])
7          if k == 0:
8              i_s = I_in[0]/s
9              u_s = U_in[0]/s
10         else:
11             i_s = i_s + (I_in[k]-I_in[k-1])/s*sym.exp(-(t_in[k]+DT)*s)
12             u_s = u_s + (U_in[k]-U_in[k-1])/s*sym.exp(-(t_in[k]+DT)*s)
13
14     return i_s, u_s
```

The parameter $g$ is only used as an implementation parameter in order to make the same equation of $U\_in$ for all the three chemical species. Moreover, the parameter $K_r$ has been defined as $K_r = N_0/4F$. The parameter $DT$ adds a time delay at the beginning of the input function in order to reach the steady state conditions of

the cell. This delay is necessary since the implementation of the input step up function consider the variable $I\_in$ and $U\_in$ null at instant zero. Therefore, during the wait time $DT$, the pressure will reach steady state in the condition that corresponds to the flow rate imposed at $t = 0$ in the input file. After $DT$, it is possible to start the effective simulation. After all the calculations, the arrays of pressures are calculated for a total time $t = DT + l$ where $l$ is the time of the simulation.

In this python function, two Laplace function are created, one for the current ($I\_in$) and the other one for the input function ($U\_in$, described in eq. 4.28) that will be multiplied to the transfer function to calculate the pressure. While the input function is used for the calculation, the current function is only calculated with Laplace to convert it from the Laplace domain to the time domain for further calculation in the *main* file.

$$U_{in,i} = \dot{q}_i - gK_r I_{in} \tag{4.28}$$

**Transfer function**

The *"pp"* function is used in order to calculate the pressure by using the transfer function described in equation 4.29. After the calculation, the result is converted to the time domain and the first $DT/dt$ elements are removed.

$$H_i = \frac{1/K_i}{\tau_i \cdot s + 1} \tag{4.29}$$

The equations 4.12, 4.13, and 4.14 are implemented in the code as in eq. 4.30.

$$p_i = H_i \cdot U_{in,i} \tag{4.30}$$

The function *pp* will return the arrays of time, current, and pressure to the func-

tion *part_press* in which, after calculating the partial pressures for all the chemical spices, will return them to the main file.

```
def pp(i_s, u_s, K, T, dt, DT, l):

    H = (1/K) / (T*s + 1)
    p_s = H * u_s

    i_t = inverse_laplace_transform(i_s, s, t)
    p_t = inverse_laplace_transform(p_s, s, t)

    res = int(1.0/dt)
    time = np.linspace(0, DT+l, res*(DT+l))
    curr = np.zeros(len(time))
    pres = np.zeros(len(time))

    for k in range(len(time)):
        curr[k] += float(i_t.subs(t, time[k]))
        pres[k] += float(p_t.subs(t, time[k]))

    time = np.linspace(0, l, res*(l))
    curr = curr[res*DT:res*DT+res*(l)]
    pres = pres[res*DT:res*DT+res*(l)]

    return time, curr, pres
```

### Calculation of the output voltage and power

Inside the main file, all the calculations of the electrochemical and thermal model are performed. Inside a *for* cycle, all the parameters are calculated, for each instant of time. At the end of the cycle, all the variables are stored in arrays that will be saved in an Excel output file (this part is not described in the document since it does not concern the model itself). In the first part of the for cycle, the voltage and power calculation are performed. Moreover, for the calculation of the voltage loss, the ASR is used and its value is determined once given the open circuit voltage, in order to fit the experimental results shown in the validation section.

```
e_ocv =  E_T + R*T[k]/(z_h2*F) * np.log((p_h2[k]*np.sqrt(p_o2[k]))/p_h2o[k])
e_loss = r * I[k]
V = N0*(e_ocv - e_loss)
P = V*I[k]
```

The calculation of the power produced is similar to the one presented in the section before, with the only difference that the open circuit voltage (*e_ocv*) and the losses (*e_loss*) are multiplied by the number of cells (*N0*) of the stack.

### 4.3.2 Thermal model

#### Calculation of the heat produced

After reading all the input variables from the input excel file, all the thermal model is performed in a for cycle that calculates all the parameters for each instant of time. Before it is necessary to scale the dimension of the stack by using the *power increase* parameter if the simulation 2 is carried out, and few other parameters are calculated before the execution of the for cycle.

```
if simulation == 2:
    N0 = N0*power_increase
    m_stk = m_stk*power_increase
    m_pcm = m_pcm*power_increase
    P_max = P_max*power_increase

T_melt = T_melt+273
Eox = 1/u_ox
q_pcm_max = h_melt * m_pcm
m_stk_pcm = m_pcm + m_stk
cp_stk_pcm = (cp_stk*m_stk+cp_pcm*m_pcm)/m_stk_pcm
```

Regarding the calculation of the heat produced, it is first necessary to calculate the molar flow rates of the chemical species that enter and exit the stack. Firstly, the equivalent mass flow rate is calculated, after all the inlet molar flow rates are

referenced to the equivalent hydrogen and are calculated as a percentage of it.

```
q_h2_i = N0*I[k]*e_f[k]/(z_h2*F)
q_h2o_i = q_h2_i * 13.2/(66.8*e_f[k])
q_o2_i = q_h2_i * Eox/(2*e_f[k])

q_h2o_o = q_h2_i * 80/(66.8*e_f[k])
q_h2_o = q_h2_i * (e_f[k]-1)/e_f[k]
q_o2_o = q_h2_i * (Eox-1)/(2*e_f[k])

q_n2 = q_h2_i * 3.76*Eox/(2*e_f[k])
q_co = q_h2_i * 13.2/(66.8*e_f[k])
q_co2 = q_h2_i * 6.8/(66.8*e_f[k])
q_air_i = q_o2_i + q_n2
```

The enthalpies for each spice are calculated by calling the function $fun\_h\_in$ and $fun\_h\_out$. After that, the enthalpy fluxes at the inlet and outlet are calculated. Then, the eq. 4.20 is implemented. In particular, both the functions use the library *"PYroMat"*, but the function $fun\_h\_in$ receive the air and fuel temperatures, that are assumed to be different. Instead, the function $fun\_h\_out$ takes only one temperature as input parameter, as the output gasses temperature are assumed to be at the same temperature of the stack.

```
    h_h2_i, h_co_i, h_co2_i, h_h2o_i, h_o2_i, h_n2_i, h_co_i, h_co2_i =
        fun_h_in(T_air, T_fuel)
    h_h2_o, h_co_o, h_co2_o, h_h2o_o, h_o2_o, h_n2_o, h_co_o, h_co2_o =
        fun_h_out(T[k])
    h_in = h_h2_i*q_h2_i + h_h2o_i*q_h2o_i + h_n2_i*q_n2 + h_o2_i*q_o2_i +
        h_co_i*q_co + h_co2_i*q_co2
    h_ut = h_h2_o*q_h2_o + h_h2o_o*q_h2o_o + h_n2_o*q_n2 + h_o2_o*q_o2_o +
        h_co_o*q_co + h_co2_o*q_co2
    h_in_loss = h_h2_i*q_h2_i + h_co_i*q_co + h_n2_i*q_n2 + h_o2_i*q_o2_i
    h_loss = (0.137*(P/P_max)*(P/P_max)-0.273*(P/P_max)+0.328)*h_in_loss
    if simulation == 0 or simulation == 1:
        q_net = h_in - h_ut - P
    elif simulation == 2:
        q_net = h_in - h_ut - P - h_loss
```

It is important to say that for simulation 0 and 1, since the stack is supposed to be adiabatic, the loss term is not included in the net heat calculation.

### Calculation of the enthalpies

The enthalpies calculation is done by using the library *"PYroMat"* in an external function.

```
def fun_h_in(T_air, T_fuel):
    pm.config['unit_energy'] = 'J'
    pm.config['unit_matter'] = 'mol'
    CO = pm.get('ig.CO')
    H2 = pm.get('ig.H2')
    CO2 = pm.get('ig.CO2')
    H2O = pm.get('ig.H2O')
    O2 = pm.get('ig.O2')
    N2 = pm.get('ig.N2')
    AIR = pm.get('ig.air')
    h_h2 = H2.h(T_fuel)
    h_co = CO.h(T_fuel)
    h_co2 = CO2.h(T_fuel)
    h_h2o = H2O.h(T_fuel)
    h_o2 = O2.h(T_air)
    h_n2 = N2.h(T_air)
    h_air = AIR.h(T_air)
    return h_h2[0], h_co[0], h_co2[0], h_h2o[0], h_o2[0], h_n2[0], h_co[0], h_co2[0]
```

### PID controller

```
if simulation == 1:
    T_setpoint = 850+273
    pid = PID(Kp=5, Ki=0, Kd=0, setpoint=T_setpoint)
    out_control = pid(T[k])
    u_ox = u_ox + out_control/4e7
    Eox = 1/u_ox
```

A PID controller is used to regulate the air inlet flow rate in order not to overcome

the maximum stack temperature. It is important to say that is it used only in simulation 1, where the step input curve for the validation is imposed. For simulation 2, the PID does not work since the PCM material is the only responsible that keep the temperature constant.

### Implementation of the PCM

The last section regards the three different modality in which the model can work. In this section, $Q_m$ represents the energy present in the PCM during phase change. It is null when the material is completely solid and equal to $Q_{sl}$ when it is completely melted. In fact, $Q_{sl}$ represents the maximum storable energy inside the PCM during the phase shift. Moreover, *cp_stk* represents the specific heat capacity of the stack and *cp_stk_pcm* represents the mean of the specific heat capacity between the stack and PCM, calculated as shown in eq. 4.31. Furthermore, before storing the data of $Q_m$ in the excel file, it has been scaled to $Q_{sl}$, to obtain the percentage of liquid present in the PCM.

$$c_{p,stk,pcm} = \frac{c_{p,stk} \cdot M_{stk} + c_{p,pcm} \cdot M_{pcm}}{M_{stk} + M_{pcm}} \tag{4.31}$$

**Mode 0** In this modality, the temperature of the stack is kept constant and the energy stored in the PCM is null, since in this modality it is not implemented.

```
if mode == 0:
    T.append(T_start)
    q_m.append(0)
    q_pcm.append(0)
```

**Mode 1** In this modality, the dynamic of temperature is implemented and the value of the temperature is calculated for each instant of the simulation by applying the eq. 4.19. Moreover, the energy stored inside the PCM remains null, since in this modality it is not implemented.

```
elif mode == 1:
    T.append(T[k] + q_net*dt/(cp_stk*m_stk))
    q_m.append(0)
    q_pcm.append(0)
```

**Model 2** In this modality, both the temperature dynamics and the PCM are implemented. To do that, the dynamic of the temperature and the phase of the PCM depends on the working temperature of the stack and the melting temperature of the PCM ($T_{melt}$). Since the PCM is implemented, *cp_stk_pcm* is used.

$T > T_{melt}$ In this case, the PCM is completely liquid and the temperature of the stack will change in time, if $Q_{net} \neq 0$. Therefore, the PCM will not be able to work as a thermal buffer. Moreover, the energy stored inside will always be equal to the maximum possible (*q_pcm_max*).

$T \simeq T_{melt}$ In this case, the PCM is working during the phase change and for that is able to absorb or release heat in order to keep the temperature of the stack constant. Even if in theory the phase change occurs when $T = T_{melt}$, since this condition cannot be achievable in the model (the two temperatures will always be different), the phase change is considered to happen when $T$ is inside the range: $[T_{melt} - T_r; T_{melt} + T_r]$. Moreover, there is the need to differentiate two cases for implementing purposes. In the first one, when $0 <= Q_m <= Q_{sl}$, the PCM works as a thermal buffer and the temperature of the stack remains constant. The second case is created for implementing purposes since the temperature range of *mode 2* is added. In fact, when $Q_m < 0$ or when $Q_m > Q_{sl}$, the PCM can not store or release energy anymore and the operating temperature will change.

$T < T_{melt}$ In this case, the PCM is completely solid and it will not act as a thermal buffer. Therefore, the operating temperature of the stack will change.

```
elif mode == 2:
    q_pcm.append(q_pcm[k] + q_net*dt)
    if T[k] > T_melt+T_r:
        T.append(T[k] + q_net*dt/(cp_stk_pcm*m_stk_pcm))
        q_m.append(q_pcm_max)
    elif T_melt-T_r <= T[k] <= T_melt+T_r:
        if 0 <= q_m[k] <= q_pcm_max:
            T.append(T[k])
            q_m.append(q_m[k] + q_net*dt)
        elif q_m[k] < 0:
            T.append(T[k] + q_net*dt/(cp_stk_pcm*m_stk_pcm))
            if T[k] < T[k-1]:
                q_m.append(q_m[k])
            else:
                q_m.append(q_m[k] + q_net*dt)
        elif q_m[k] > q_pcm_max:
            T.append(T[k] + q_net*dt/(cp_stk_pcm*m_stk_pcm))
            if T[k] > T[k-1]:
                q_m.append(q_m[k])
            else:
                q_m.append(q_m[k] + q_net*dt)
    elif T[k] < T_melt-T_r:
        T.append(T[k] + q_net*dt/(cp_stk_pcm*m_stk_pcm))
        q_m.append(0)
```

## 4.4 Model validation

The model validation is based on a study conduced by D'Andrea et al. [59] that analyses the thermal behavior of a biogas-fed SOFC plant. In the study, an electrochemical and thermal dynamic model is used to simulate a 1900W SOFC stack system with an external reformer that is used to reform $CH_4$. Moreover, it is validated by data provided by the SOFC manufacturer (in table 4.1) and by results collected during test that were performed during the SOFCOM proof-of-concept operation. Moreover, the inlet air temperature is $T_{air,in} = 650°C$; the inlet fuel temperature is $T_{fuel,in} = 750°C$; the stack mass is $m_{stk} = 50kg$; the specific heat of

the stack is $c_{p,stk} = 600 J/kgK$; and the stack is composed by 90 cells. The SOFC stack model is developed under the following conditions:

1. The stack is composed only by the PEN;
2. The stack is adiabatic (the loss term is added only in simulation 2);
3. The fed gas is reformed $CH_4$.

| I [A] | V [V] | P [W] | $Q_{air}$ [Nl/min] | $Q_{H_2}$ [Nl/min] | T [°C] |
|---|---|---|---|---|---|
| 24 | 62 | 1500 | 210-235 | 20.1 | 855 |
| 29 | 58 | 1680 | 315-330 | 24.1 | 855 |
| 34 | 55 | 1880 | 400 | 28 | 862 |

***Table 4.1:*** *Data provided by the manufacturer.*

In order to validate the model, a simulation with the three inlet fuel steps represented in table 4.1. The entire simulation has a length of 60 hours and each 20 hours the inlet fuel is increase of a single step. The results are the compared with the ones given by the manufacturer.

In figure 4.2 are represented the simulated voltage and the temperature trend with a straight line and the referenced one with a dashed line. It is possible to observe a good correlation between the simulation and the values given by the manufacturer. In particular, the voltage present a higher error at high load while the temperature is regulated by the PID controller and for that reason it remains under the limit of 860°C. In figure 4.3 are represented the simulated power and inlet air trend with a straight line and the referenced one with a dashed line. Also in this figure, a good correlation between the simulation and the data provided by the manufacturer is observed.

The model is validated also by comparing the simulated polarization curve with the one obtained by tests performed by D'Andrea et al. with the SOFCOM proof-of-concept. In figure 4.4 is represented the comparison of voltage and temperature

between the simulation (straight lines) and the tests. It is possible to observe that the correlation between simulation and tests presents high errors in the voltage curve at low load. The temperature dynamic shows the same increasing trend of the tests, even if the value reached at high load is lower than the tests.

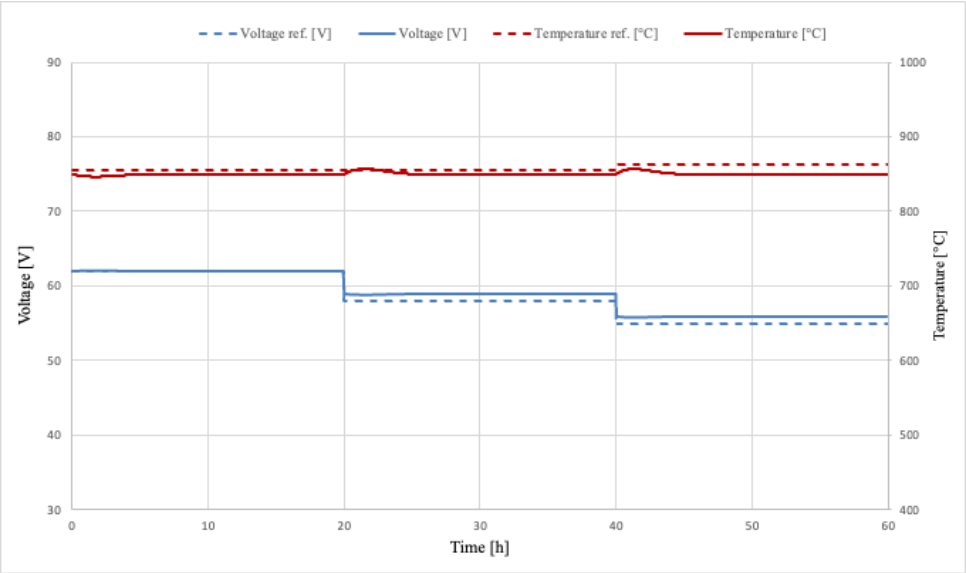


**Figure 4.2:** Voltage and Temperature validation.

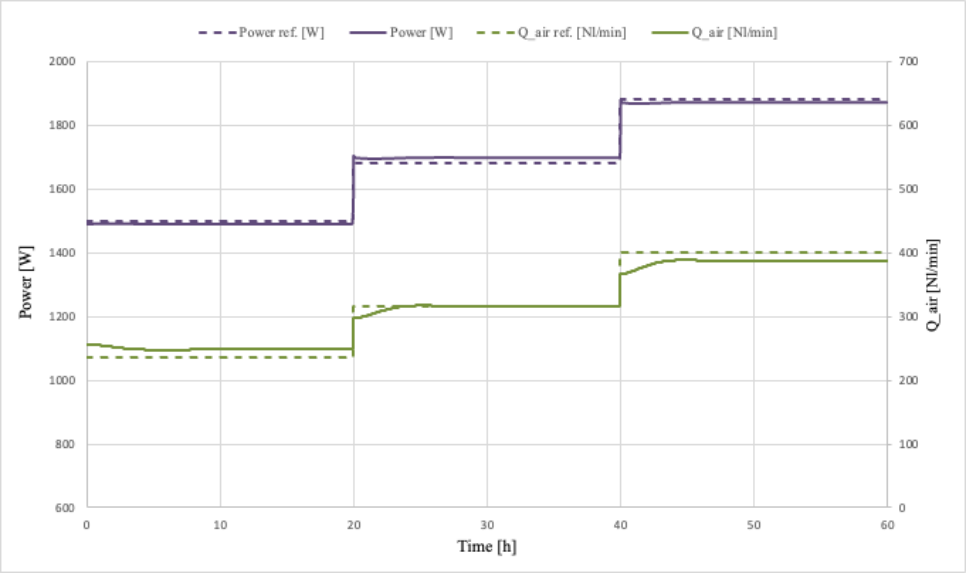


**Figure 4.3:** Power and inlet air flow validation.

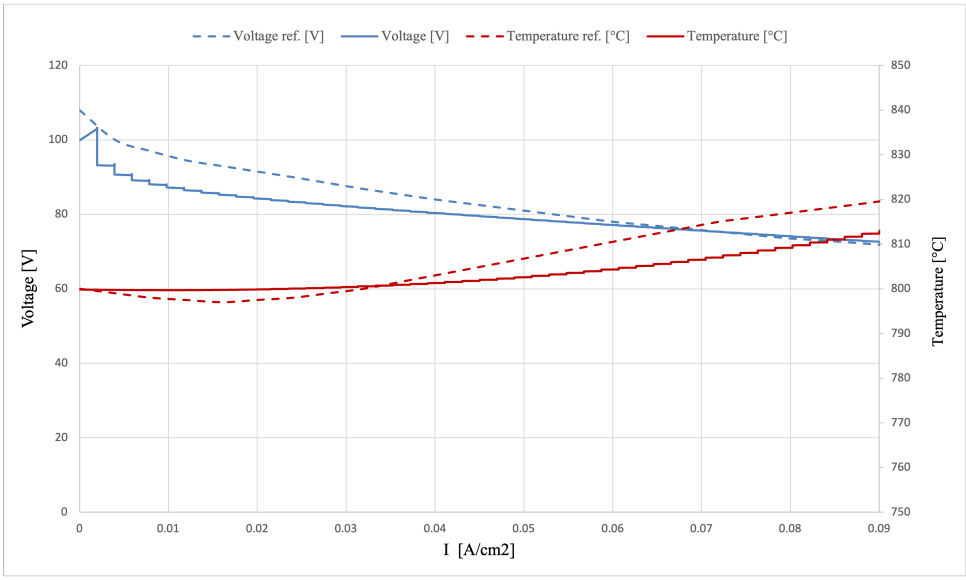


**Figure 4.4:** Polarization curve validation.

Overall, the model validation shows a good response at high load with higher errors at low load. Nevertheless, the model can be use for the purpose of the study since its aim is to analyze the SOFC stack behavior at high load.

# Chapter 5

# Results and final discussion

In order to test the model in a real-case scenario, three load profiles of a real ship covering short-distance routes were obtained from NEPTEC. In particular, the three load profiles are the following:

1. Total duration of 45 minutes, with low intensity power peaks (fig. 5.1);
2. Total duration of 45 minutes, with high intensity power peaks (fig. 5.2);
3. Total duration of 110 minutes, with low intensity power peaks (fig. 5.3);

Even if the engine delivered power goes from 0kW to a maximum of 32.4kW, all the simulations are performed by increasing the stack rated power to 60kW. In this way, the SOFC stack works between 46% and 100% of its rated power. This conditions are chosen because the loss term is experimentally evaluated by Barelli et al. [52] only in the range between 46% and 100% of the maximum power.

All the simulations are done with a generic PCM ($c_p = 0.5kJ/kgK$; $h_{melt} = 200kJ/kg$; $T_{melt} = 850°C$) are carried out by using a parameter called *"fraction of storable heat"* that is defined as in equation 5.1. This parameter permits to decouple the type of PCM material and the SOFC stack. In this way, all the simulations are independent from the type of PCM that can be chosen. Moreover, a $T_{melt} = 850°C$

has been chosen in order to maintain the SOFC stack temperature same as the validation operating conditions.

$$FSH = \frac{m_{pcm}[kg] \cdot h_{melt,pcm}[J/kg]}{P_{rated}[W]} \tag{5.1}$$

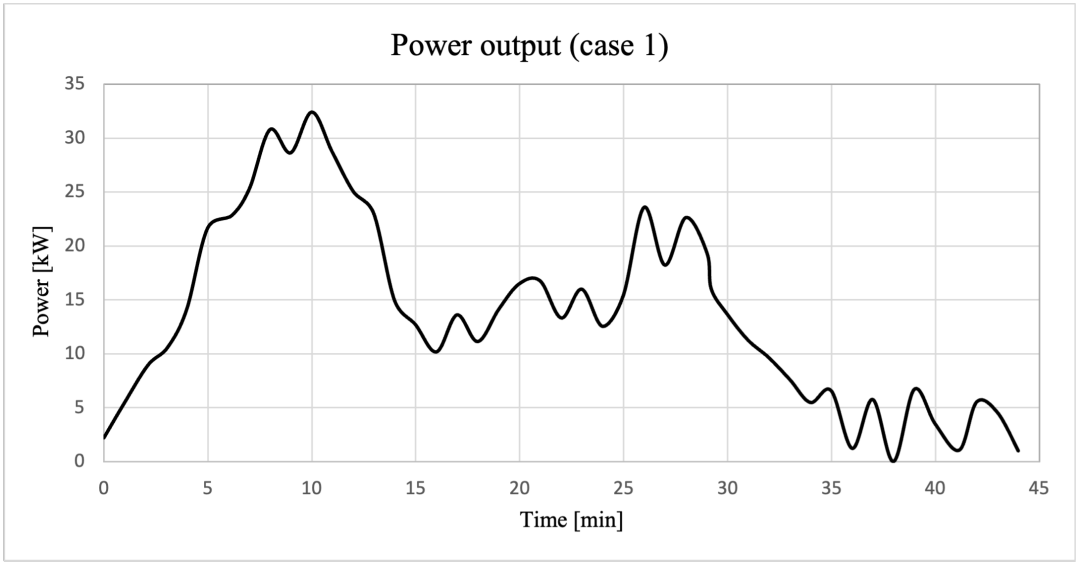


**Figure 5.1:** Power delivered by the engine of the ship (NEPTEC).

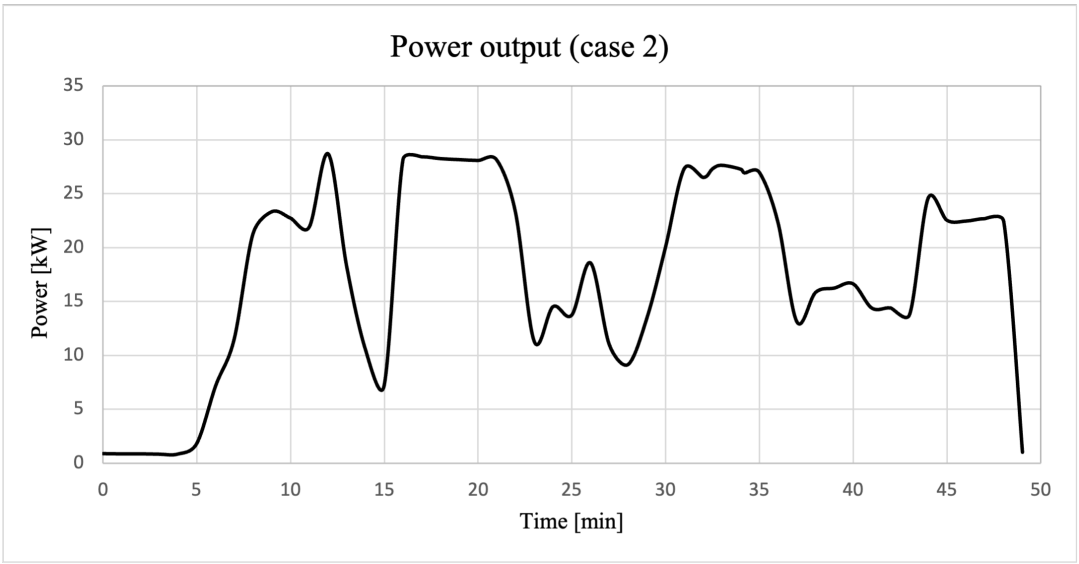


**Figure 5.2:** Power delivered by the engine of the ship (NEPTEC).

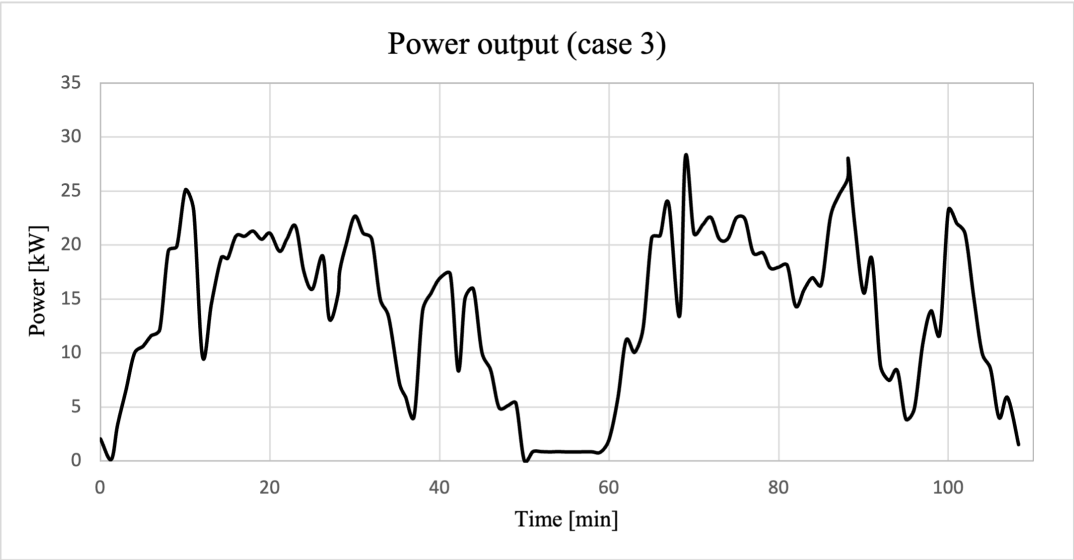


**Figure 5.3:** Power delivered by the engine of the ship (NEPTEC).

## 5.1 SOFC stack without PCM

The output power in $1^{st}$ case scenario (fig. 5.1) is characterized by a strong peak at the beginning, with an overall decreasing trend after the initial peak. The temperature dynamic without PCM is represented in figure 5.4.

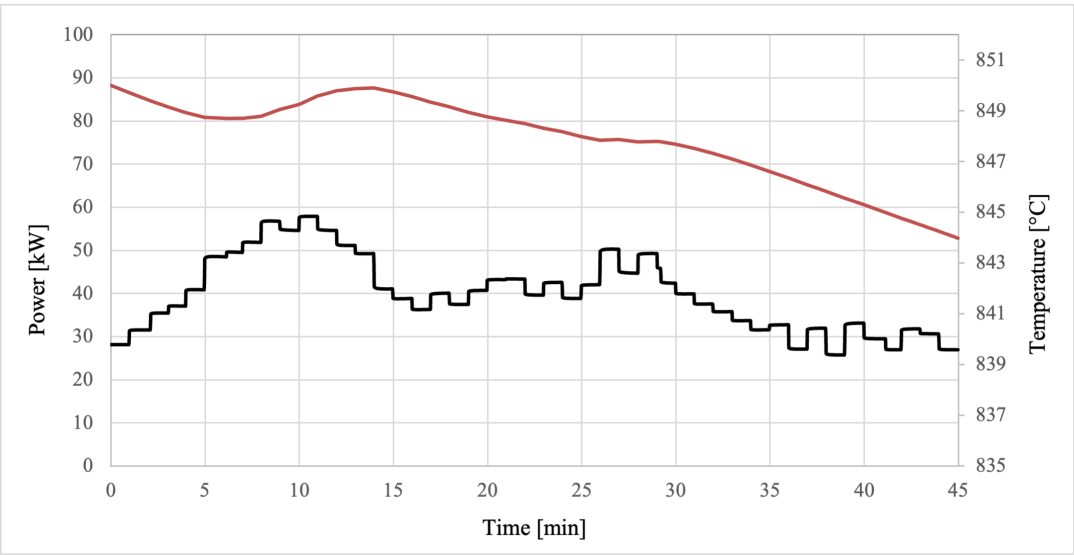


**Figure 5.4:** Stack power and temperature dynamic.

In the $2^{nd}$ case scenario the power output trend of the second scenario is longer than that of the first. In fact, it represents not only one single trip, but also the one to come back to the same river side. In particular, it is divided into two different phases with a break of 10 minutes in the middle, in which the power produced is strongly reduced. The temperature dynamic without PCM is represented in figure 5.5.

In the $3^{rd}$ case scenario a high power demand is required, which leads to a more significant increase in stack temperature, compared to the other two cases. This high increase makes the amount of PCM used in the previous cases not sufficient to mitigate all the load fluctuations. The temperature dynamic without PCM is represented in figure 5.6.

Overall, it is possible to observe that in all three cases the temperature tends to decrease along time. This common trend can be explained by looking at the quantity of air that is entering the SOFC stack. In particular, the oxidant utilization is fixed during time for all the three cases in order to maintain the stack temperature constant at a higher power compared to the power output given by NEPTEC.

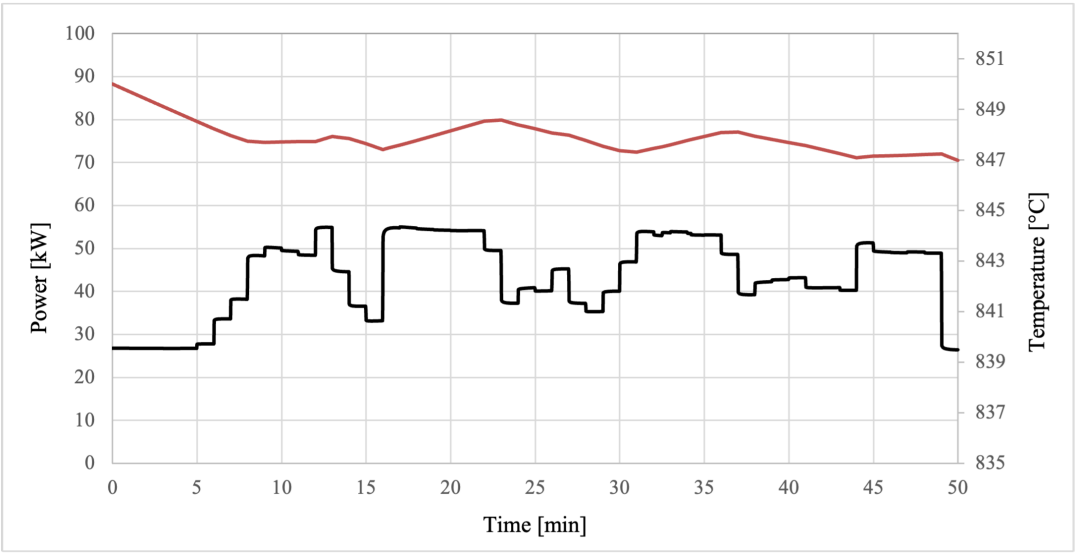


**Figure 5.5:** Stack power and temperature dynamic.

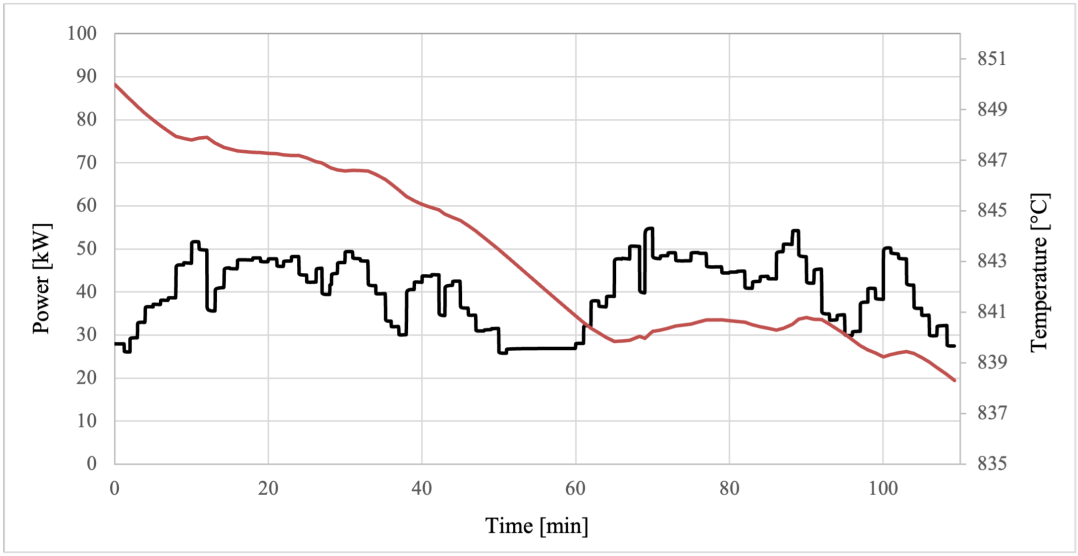


**Figure 5.6:** Stack power and temperature dynamic.

## 5.2 Implementation of the PCM in the stack

In this section the PCM material is implemented inside the SOFC stack. All the simulations are carried out for all the three different cases scenario given by NEPTEC. The aim of this section is to study the influence of the amount of PCM (by imposing the FSH), the travel time, the initial liquid fraction, and the oxidant utilization. Moreover, the fuel utilization is fixed to 0.75.

### 5.2.1 Influence of the FSH

In order to study the influence of the PCM quantity in the SOFC stack, the simulations are carried out by fixing the liquid fraction to 0.2 and by increasing the FSH. For each case scenario, different values of FSH are considered and are summed up in table 5.1. For the $1^{st}$ and $2^{nd}$ cases, the FSH chosen are quite similar, while for the $3^{rd}$ case it increase due to the longer travel duration. The results of the simulations are shown in figure 5.7, 5.8, 5.9 for the three different case scenario.

| | $FSH_1$ | $FSH_2$ | $FSH_3$ | $FSH_4$ |
|---|---|---|---|---|
| *Case 1* | 120 | 240 | 360 | 480 |
| *Case 2* | 80 | 160 | 240 | 320 |
| *Case 3* | 300 | 600 | 900 | 1200 |

***Table 5.1:*** *Different values of FSH for each tested case scenario.*

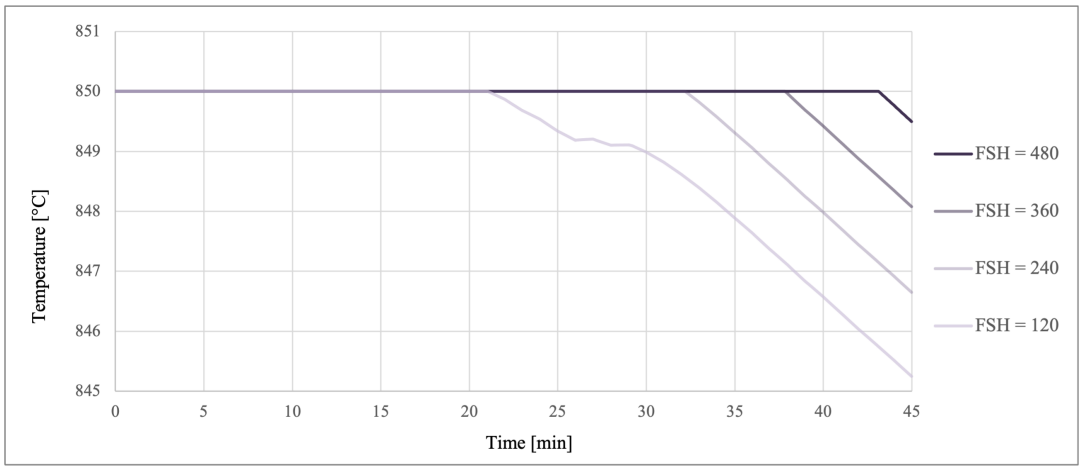


**Figure 5.7:** Temperature dynamic for different FSH (case 1).

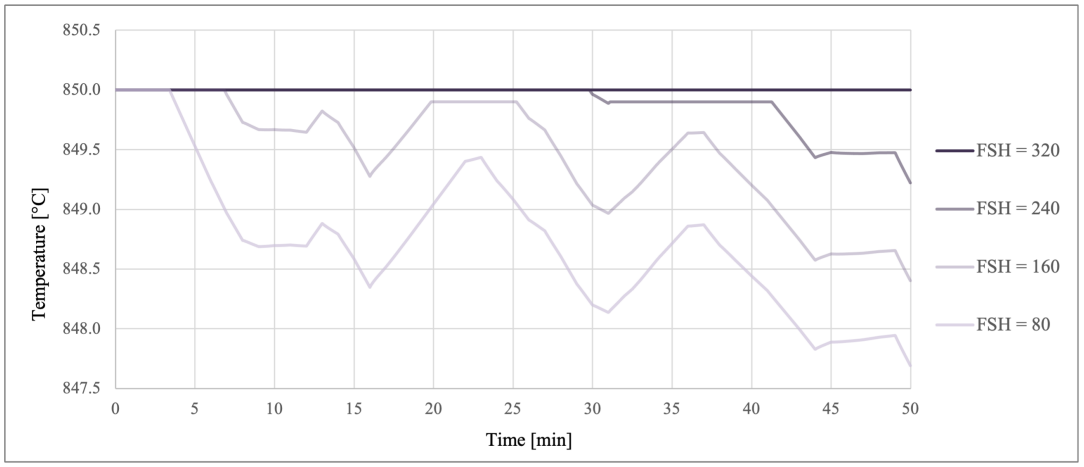


**Figure 5.8:** Temperature dynamic for different FSH (case 2).

In the results it is possible to observe that for low values of FSH the temperature decreases under the setpoint. At the beginning of the simulation, the PCM is able

to face the load variations by releasing or absorbing heat. After an initial time, the temperature shows a reduction since the PCM, completely solid, can not absorb heat anymore. For that reason, the temperature starts to have a drop that become lower by increasing the FSH.

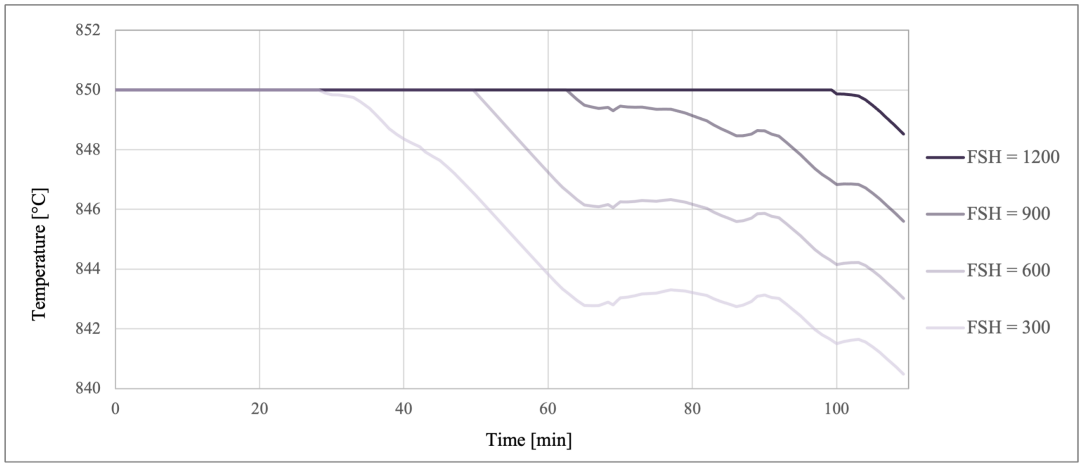


**Figure 5.9:** Temperature dynamic for different FSH (case 3).

### 5.2.2 Influence of the travel time

To analyze the influence of travel time on the stack dynamic, the three cases scenario are increased in time by multiplying all the time steps by a factor that goes from 1 to 10 for the first two cases and form 1 to 5 in the third case. Each simulation has been carried out by imposing an initial liquid fraction of 0.5 and a fraction of storable heat of 120, 80, and 300 for the three cases. The temperature dynamic in the three cases is shown in figure 5.10, 5.11 and 5.12.

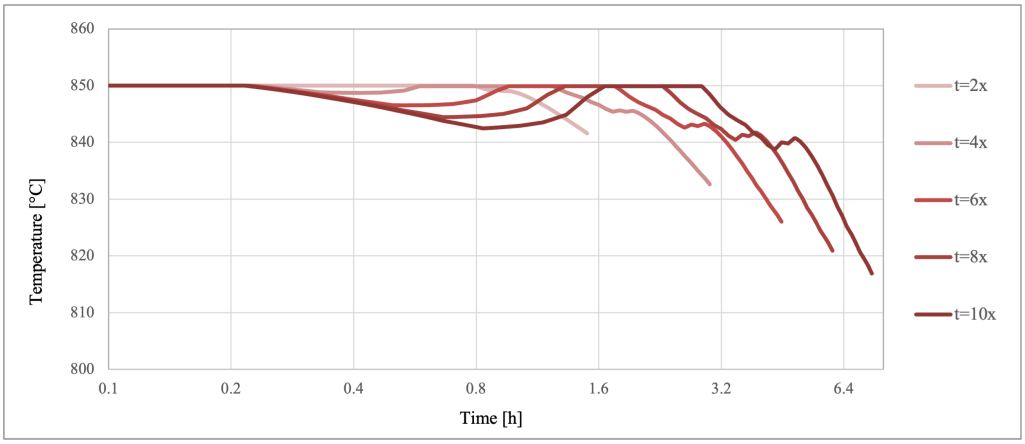


**Figure 5.10:** Temperature dynamic for different travel time duration (case 1).

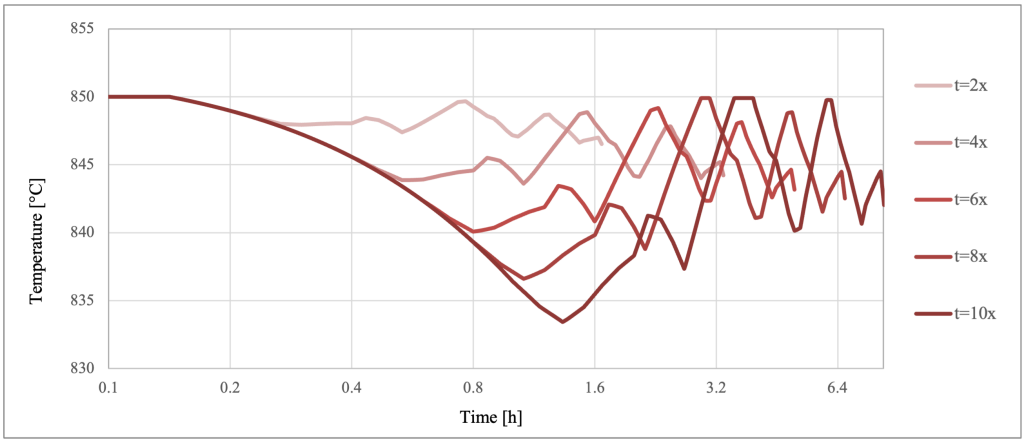


**Figure 5.11:** Temperature dynamic for different travel time duration (case 2).

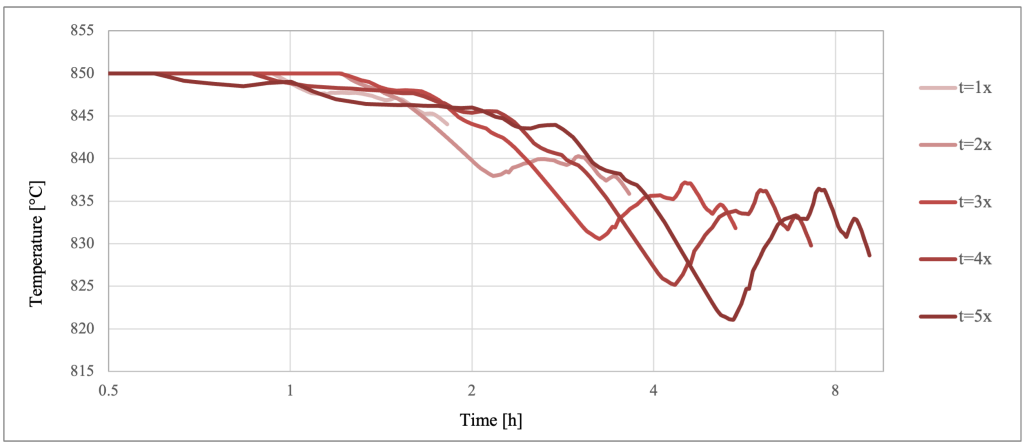


**Figure 5.12:** Temperature dynamic for different travel time duration (case 3).

The temperature dynamic for all three cases shows a decrease after less than one hour of travel time due to the PCM limited capacity. In addition, the increase in time lead to a higher temperature reduction, which goes until 820°C in the third case, after 7 hours of travel time.

### 5.2.3 Influence of the initial liquid fraction

The initial liquid fraction correspond to the amount of liquid of the PCM when it works in the phase change area and it has a strong influence on the thermal dynamic of the SOFC stack. To analyze its influence, the simulations were done by varying the initial liquid fraction from 0.2 to 0.8 with steps of 0.2 while the FSH was fixed to 120, 80, and 300 for each case. The simulations results are shown in figure 5.13, 5.14, and 5.15.

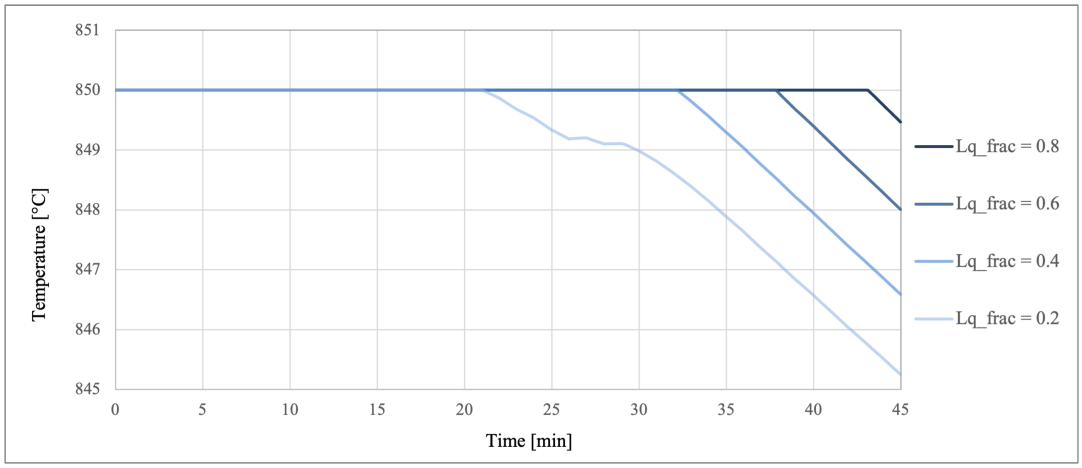


**Figure 5.13:** Temperature dynamic for different initial liquid fraction (case 1).

The results highlight a temperature decrease after an initial time in which the temperature is constant. Overall, the initial time decrease and the temperature drop increase when the initial liquid fraction is reduced. Moreover, the temperature dynamic, for each case, presents a trend that is the same of the cases with fixed liquid fraction and variable FHS. This similar trend is due to the limited capacity of the PCM release heat when the output power needed. For low values of FSH or

liquid fraction, the temperatures start to decrease after an initial time of a $\Delta T$ that increases when FSH and liquid fraction lowers.

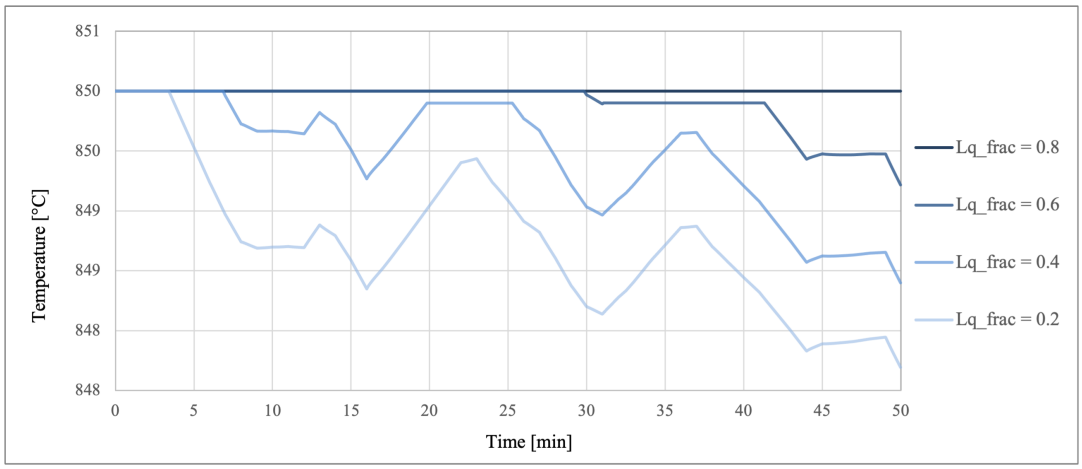


**Figure 5.14:** Temperature dynamic for different initial liquid fraction (case 2).

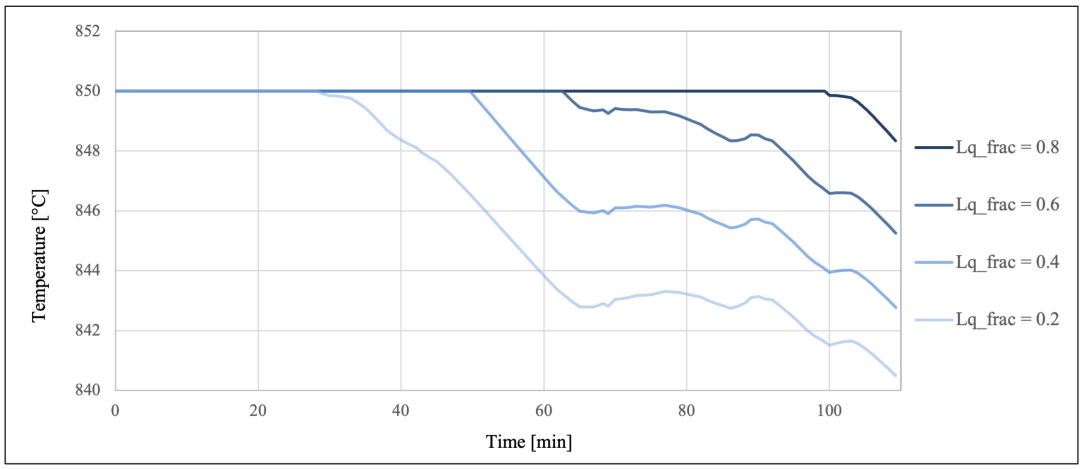


**Figure 5.15:** Temperature dynamic for different initial liquid fraction (case 3).

### 5.2.4 Influence of the oxidant utilization

The oxidant utilization factor (eq. 4.23) is the ratio between the stoichiometric oxygen needed for the reaction and the total one inside the cathode. An increase of this factor lead to lower oxygen excess and, as a consequence, less air cooling effect. $U_{ox}$ remains constant during all the simulation, while the stoichiometric oxygen

change depending on the power output. Moreover, for all the simulations, the initial liquid fraction is imposed to 0.5 and the FSH is 120, 80 and 300 for the three cases.

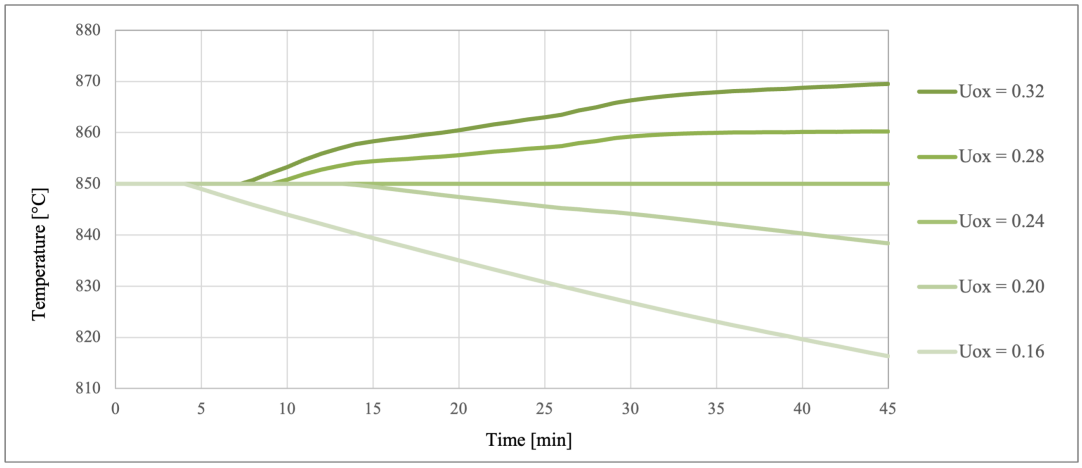


**Figure 5.16:** Temperature dynamic for oxidant utilization (case 1).

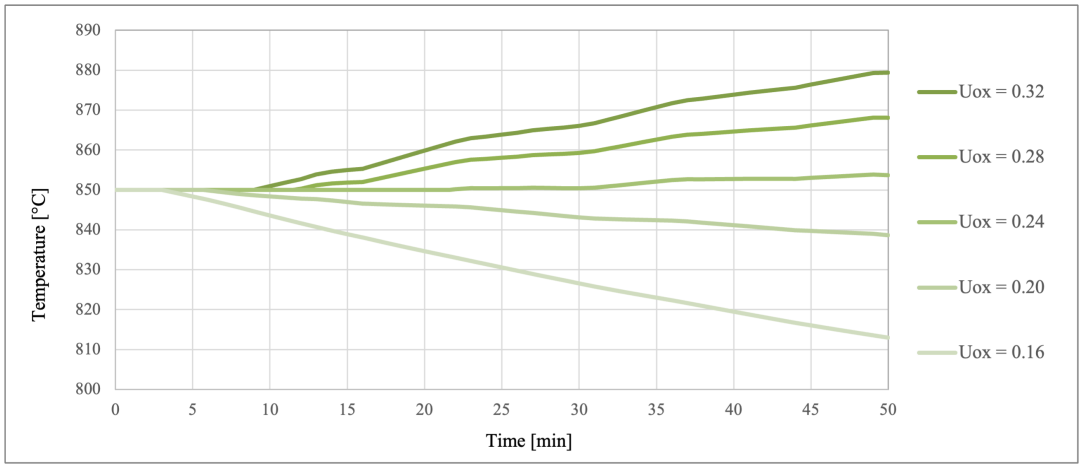


**Figure 5.17:** Temperature dynamic for oxidant utilization (case 2).

The results shown in figure 5.16, 5.17, and 5.18, indicate that the temperature strongly depends on the oxidant utilization factor. For example, a small change of 0.02 in the third case, from 0.16 to 0.18, lead to 20°C of different of the stack temperature at the end of the simulation. As expected, the stack temperature decreases for low value of $U_{ox}$, while it increase when the oxidant utilization increase. For that reason, the choice of the value of this parameter is important to keep the

stack temperature constant.

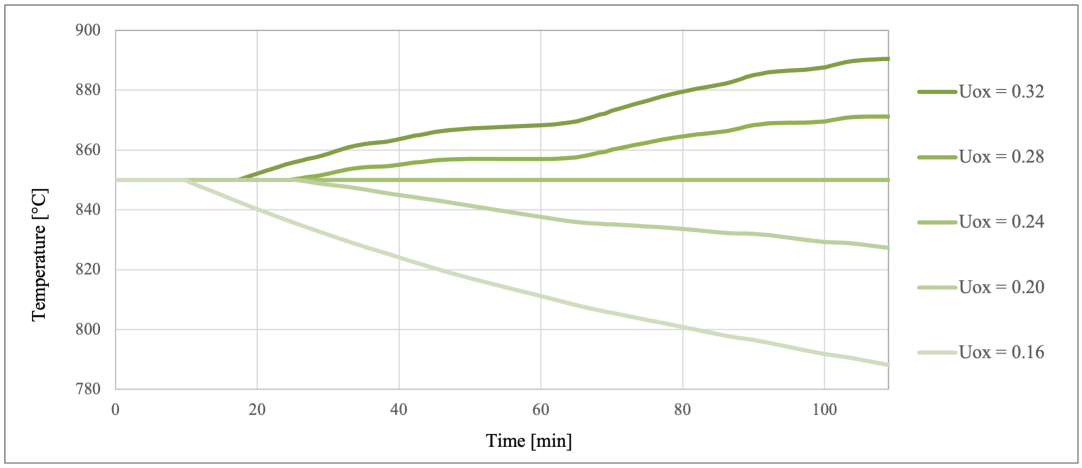


**Figure 5.18:** Temperature dynamic for oxidant utilization (case 3).

### 5.2.5 Influence of the operating temperature

In order to test the influence in the operating temperature ($T_{stack}$), it has been changed from 850°C to 810°C with step of 10°C for each case scenario. The $U_{ox}$ was fixed to 0.22 and the initial liquid fraction to 0.5. Regarding the PCM, the FSH was set to 120, 80, and 300 for the three cases and the melting temperature reduced in each simulation in order to be the same as the operating temperature. Moreover, the fuel and air inlet temperature are kept to 750 and 650. Consequently, by changing the operating temperature of the SOFC stack, and so the enthalpies of the outlet gasses, the cooling effect of air and fuel decrease when the stack operating temperature decrease. For that reason, a higher generated heat ($Q_{net}$) is expected.

The simulations results are represent in term of $Q_m$, that is the heat stored in the PCM. In particular $Q_m = 0$ is set in correspondence of the beginning of the phase change, when the material is completely solid. Values of $Q_m$ under zero represent a situation in which the PCM is not anymore capable of releasing heat to keep the temperature constant, and the stack temperature start to decrease. On the contrary, then $Q_m$ goes above $Q_{pcm,max} = m_{pcm} \cdot h_{melt}$, the PCM is not capable

anymore of absorbing the extra-heat and the stack temperature starts to increase. The choice of this representation is motivated by the fact that not in all cases the stack temperature change, but only in the third case.

The simulation results in all cases, represented in figure 5.19, 5.19 and 5.20, shows that a decrease in the stack temperature lead to a higher $Q_{net}$ that tends increase $Q_m$ in time. Moreover, during all the simulation, $Q_m$ exceed the boundaries of zero and $Q_{pcm,max}$ for some operating temperatures, and, has a consequence, the PCM does not operate in the phase change. For that reason the stack temperature is not maintained constant.

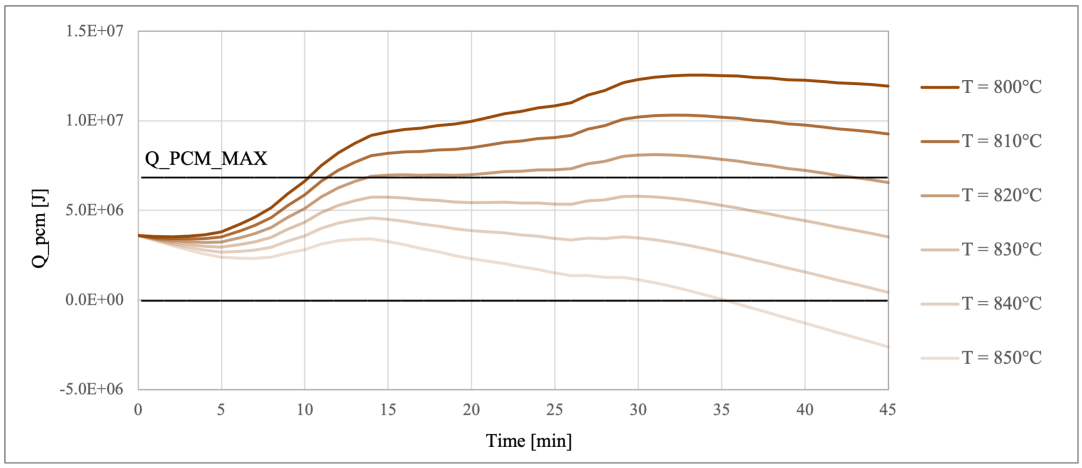


**Figure 5.19:** Stored heat dynamic for different operating temperatures (case 1).

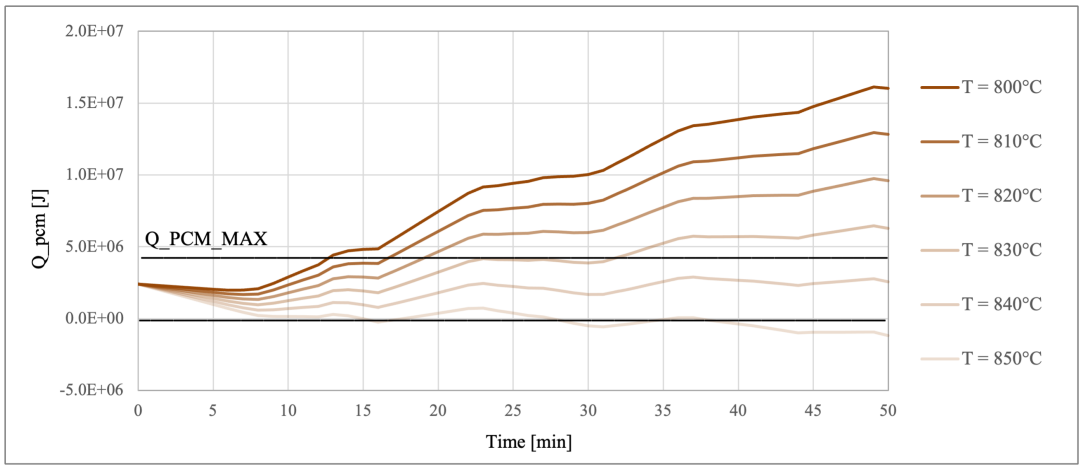


**Figure 5.20:** Stored heat dynamic for different operating temperatures (case 2).

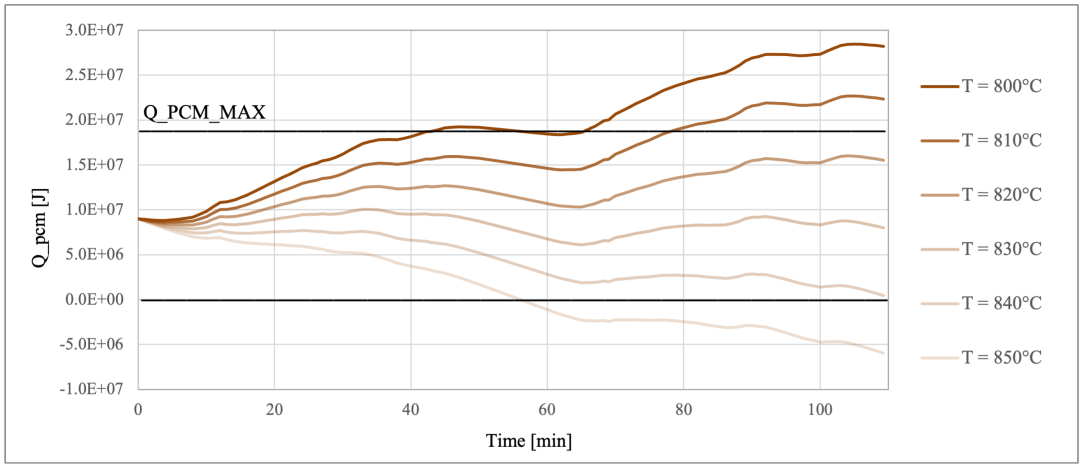


**Figure 5.21:** Stored heat dynamic for different operating temperatures (case 3).

## 5.3 Integration of the three case scenario

The following analysis aims to see how the stack response to all the three cases together, as shown in the power output in figure 5.22.

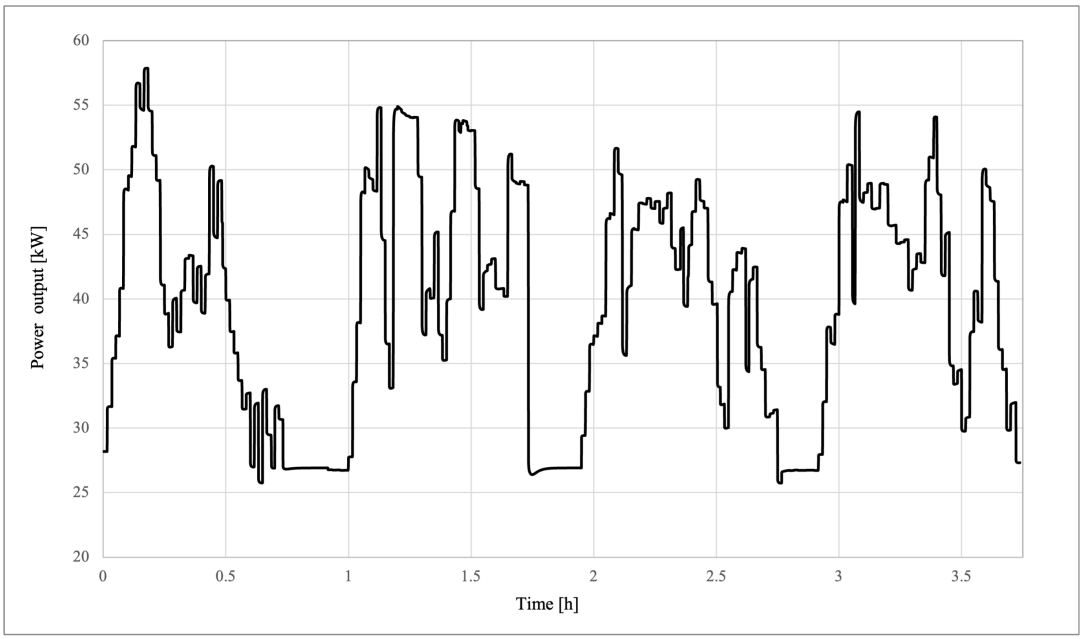


**Figure 5.22:** power output of the three cases scenario together.

Since the original power output given by NEPTEC correspond to an engine

mounted on small cruise ship that cross a river, the simulated scenario correspond to a ship that cross a river four consecutive times. Between each trip, the ship attend around 10 minutes in the riverbank before the next trip.

Differently from the cases in the section before, all the results of the simulations are shown only in the cases in which the temperature is constant, in order to see the range of values that permits the optimize the working operation in order to keep the temperature constant. The fuel utilization is fixed to 0.75 and the maximum power to $60kW$, as in the single cases described in the sections before.

Since the temperature remains constant in each simulation, the results are shown in term of liquid fraction of the PCM during time. The parameters that has been changed are: the oxidant utilization factor, the FSH, and the initial liquid fraction.

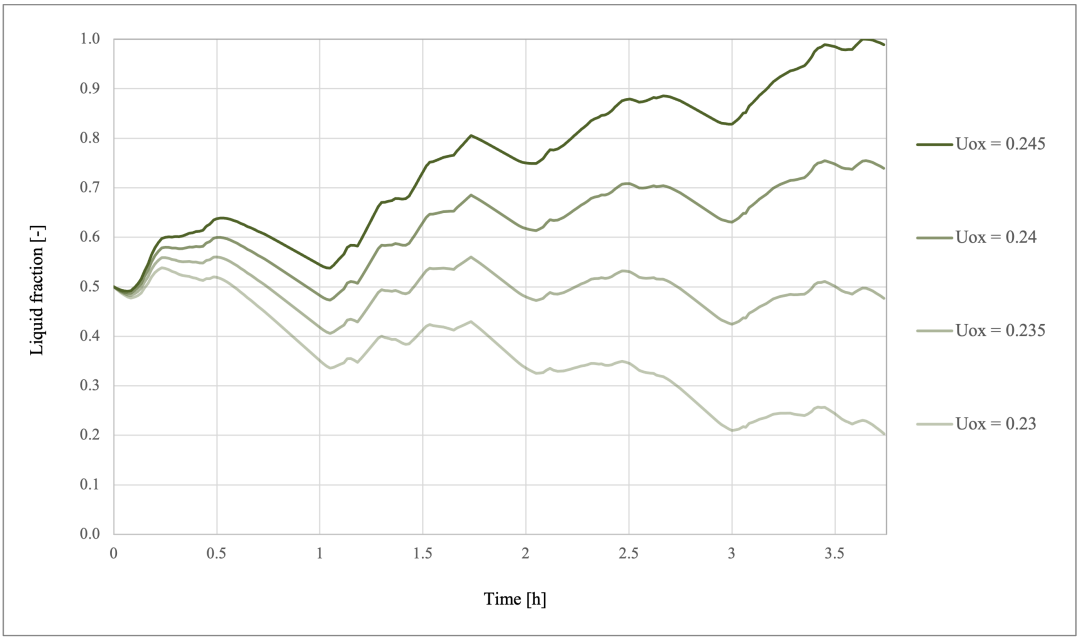


**Figure 5.23:** Variation of oxidant utilization factor.

In figure 5.23 is shown the liquid fraction for different values of $U_{ox}$. In this case, the FSH is fixed to 20 and the initial liquid fraction to 0.5. High value of $U_{ox}$ lead a less excess of air and, as a consequence, a lower cooling effect by the air. Given the power output, the liquid fraction of the PCM tend to increase since it absorbs

more heat. On the contrary, low values of $U_{ox}$ lead to high air excess and so higher cooling effect. Since the air is absorbing more heat generated by the SOFC stack, the liquid fraction decrease and the amount of solid in the PCM increase.

In figure 5.24 is shown in the liquid fraction variation for different values of FSH. In this simulations, the $U_{ox}$ is fixed to 0.235 and the initial liquid fraction to 0.5. The results show that for low values of liquid FSH, the liquid fraction variation increases, with a difference between the lower and upper peak of 0.6. On the contrary, high values of FSH lead to lower liquid fraction oscillation between the initial value.

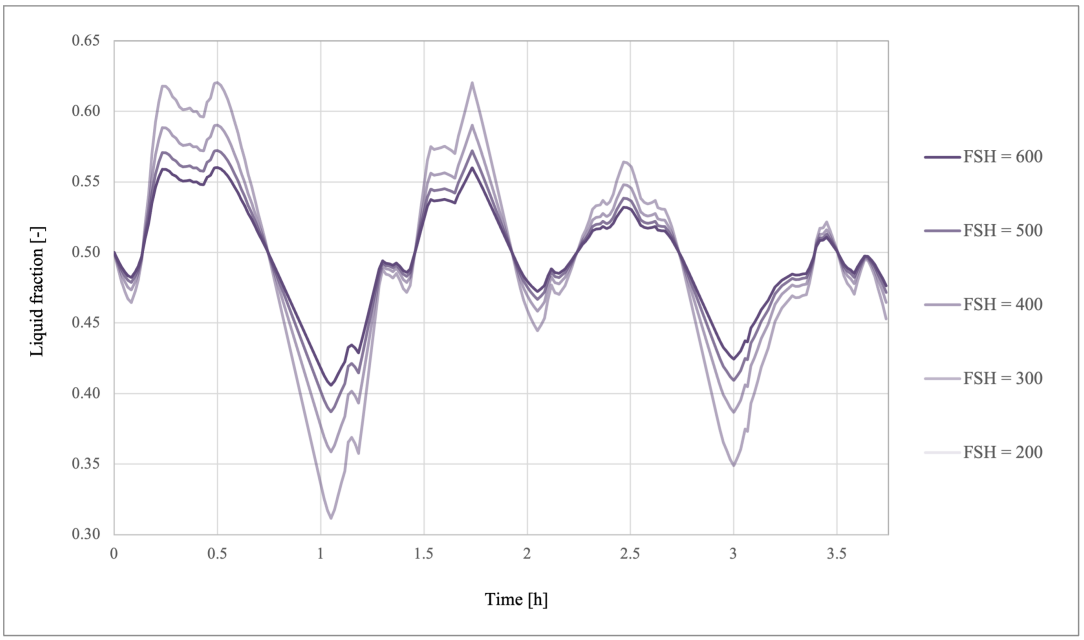


**Figure 5.24:** Variation of the FSH.

In figure 5.25 is shown the liquid fraction in function of time for different values of initial liquid fraction. In all the simulations, the FSH was fixed to 20 and the $U_{ox}$ to 0.235. The results highlight the same liquid fraction trend, that remain the same for all the initial values. Since the generated heat is the same in all cases, the absorbed and released heat for each instant of time, remain the same. For that reason, the liquid fraction trend is not dependent on the initial value if the material is capable of facing all the heat fluctuations due to the load variations.

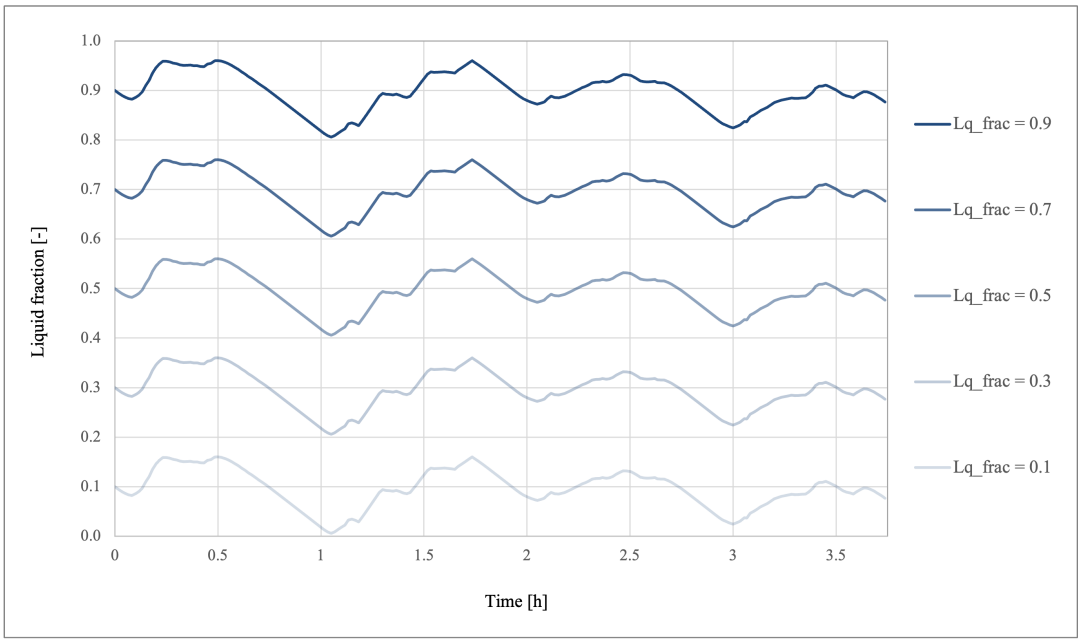


**Figure 5.25:** Variation of the initial liquid fraction.

### 5.3.1 Influence of the PCM type

All the simulations done until this section, were performed with PCM whose characteristics were not of a real material. The PCM mass was calculated after imposing the FSH. The aim of this section is to simulates the SOFC stack integrated with different metallic PCMs that already exist in the market, as listed in table 3.1. All the tested PCM are represented in table 5.2 with the mass value in kg in function of FSH. Moreover, the SOFC stack mass is $1580kg$.

All the simulations are performed with an initial liquid fraction of 0.5 and with $FSH = 600$. Since the aim of the PCM is to prevent temperature fluctuations, the stack operating temperature has been adapted to the melting temperature of the PCM, for every tested material. Moreover, since the operating temperature changes, it was necessary to change the $U_{ox}$ for each tested PCM, as shown in table 5.2. In particular, by reducing the operating temperature, more excess of air was necessary (lower $U_{ox}$). On the contrary, higher operating temperature lead to less excess (higher $U_{ox}$).

| **Compound/FSH** | $T_{melt}$ [°C] | $U_{ox}$ | **150** | **300** | **450** | **600** |
|---|---|---|---|---|---|---|
| **A)** $Al_{12.2}CU_{79.9}Mg_{7.9}$ | 812 | 0.205 | 48 | 96 | 144 | 191 |
| **B)** $Cu_{90.5}Si_{9.5}$ | 820 | 0.211 | 90 | 180 | 270 | 360 |
| **C)** $Cu_{40.3}Zn_{59.7}$ | 836 | 0.225 | 53 | 106 | 159 | 212 |
| **D)** $Cr_{1.1}Cu_{63.9}Mn_{35.0}$ | 864 | 0.245 | 60 | 120 | 180 | 240 |
| **E)** $Al_{45}Si_{40}Fe_{15}$ | 869 | 0.25 | 16 | 32 | 48 | 64 |
| **F)** $Ni_{27.8}Zn_{72.2}$ | 881 | 0.26 | 33 | 66 | 100 | 133 |

***Table 5.2:*** *Metallic PCMs mass [kg] for different values of FSH.*

As shown in figure 5.26, all the tested PCM with same FSH were able to face all the load changes, by maintaining the temperature constant. The fluctuations around the initial liquid fraction differs from one PCM to another due to the air amount, that is regulated by the $U_{ox}$ and depends on the load. For that reason, a precise control in the air quantity is still necessary, despite the presence of the PCM.

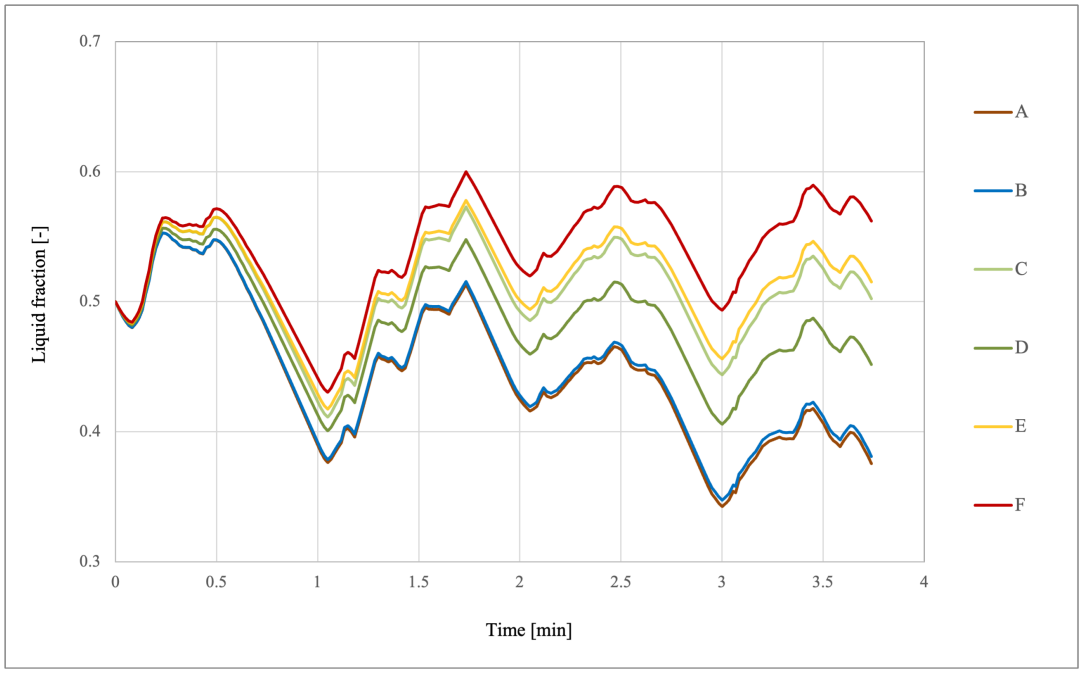


**Figure 5.26:** Change of PCM type.

Moreover, the values of initial liquid fraction has been chosen to 0.5 since it represent the point in the middle of the phase change. Nevertheless, in the choice of the amount of PCM, it is necessary to take in to account that the initial liquid fraction can differs from the value chosen in this study.

# Chapter 6

# Conclusions and future research

The overall result of the model simulations permits to demonstrate that the necessity of the managing temperature fluctuation of SOFC due to load variation can be fulfilled with the implementation of a metallic phase change material inside a SOFC stack. Thanks to load profiles acquired on a ship that covers small distances, it was possible to analyze the thermal behavior of the system SOFC/PCM under a real case scenario. The simulations reveal the need for thermal management and the effectiveness of the PCM in addressing it. By the implementation of the PCM the advantage of power output flexibility has been achieved.

However, the stack thermal response is influenced by many factors, affecting the amount of PCM that is necessary to keep the operating temperature constant. Some external factors, like the trip conditions, and some other more internal, like the operating temperature of the stack or the oxygen utilization, can strongly affect the capability of the PCM to work as a thermal buffer. Among the three different cases scenario that has been analyzed, the simulations show that it was possible to cover all the thermal fluctuations by implementing a PCM inside the SOFC stack with a FSH = 600, with an operating temperature equal to the melting temperature of the PCM.

Future studies can be done in order to improve the model capability to predict

the system SOFC stack/PCM response to load changes. In particular, the impact of geometry can be examined as it is not considered in the model's current state. Moreover, the reactivity of the PCM is still not taken in to account. In fact, in the results presented, the PCM react instantly in response to the load change, without any considered delay.

# Bibliography

[1] Nur Syafkeena Mohd Affandi and Nafisah Osman. "Short review on global trends in SOFC scenario and future perspective". In: *Materials Today: Proceedings* 66 (2022), pp. 3981–3984. ISSN: 2214-7853.

[2] Francesco Baldi et al. "A Cogeneration System Based on Solid Oxide and Proton Exchange Membrane Fuel Cells With Hybrid Storage for Off-Grid Applications". In: *Frontiers in Energy Research* 6 (Jan. 2019). ISSN: 2296-598X.

[3] Sanaz Zarabi Golkhatmi, Muhammad Imran Asghar, and Peter D. Lund. "A review on solid oxide fuel cell durability: Latest progress, mechanisms, and study tools". In: *Renewable and Sustainable Energy Reviews* 161 (June 2022), p. 112339. ISSN: 1364-0321.

[4] Jingxuan Peng et al. "Solid oxide fuel cell (SOFC) performance evaluation, fault diagnosis and health control: A review". In: *Journal of Power Sources* 505 (Sept. 2021), p. 230058. ISSN: 0378-7753.

[5] A.S. Mehr et al. "Polygeneration systems based on high temperature fuel cell (MCFC and SOFC) technology: System design, fuel types, modeling and analysis approaches". In: *Energy* 228 (2021), p. 120613. ISSN: 0360-5442.

[6] Junhan Cheng et al. “Crossflow flat solid oxide fuel cell (SOFC) semi-empirical modeling and the multi-fuel property based on a commercial 700 W stack”. In: *Fuel* 358 (Feb. 2024), p. 130172. ISSN: 0016-2361.

[7] Qidong Xu et al. “A comprehensive review of solid oxide fuel cells operating on various promising alternative fuels”. In: *Energy Conversion and Management* 253 (Feb. 2022), p. 115175. ISSN: 0196-8904.

[8] L.S. Mahmud, A. Muchtar, and M.R. Somalu. “Challenges in fabricating planar solid oxide fuel cells: A review”. In: *Renewable and Sustainable Energy Reviews* 72 (May 2017), pp. 105–116. ISSN: 1364-0321.

[9] Zezhi Zeng et al. “A review of heat transfer and thermal management methods for temperature gradient reduction in solid oxide fuel cell (SOFC) stacks”. In: *Applied Energy* 280 (Dec. 2020), p. 115899. ISSN: 0306-2619.

[10] Shichuan Su et al. “Anode-Versus Cathode-Supported Solid Oxide Fuel Cell: Effect of Cell Design on the Stack Performance”. In: *International Journal of Electrochemical Science* 10.3 (Mar. 2015), pp. 2487–2503. ISSN: 1452-3981.

[11] Milad Ebadi Chelmehsara and Javad Mahmoudimehr. “Techno-economic comparison of anode-supported, cathode supported, and electrolyte supported SOFCs”. In: *International Journal of Hydrogen Energy* 43.32 (Aug. 2018), pp. 15521–15530. ISSN: 0360-3199.

[12] C. Berges et al. “Fused filament fabrication for anode supported SOFC development: Towards advanced, scalable and cost-competitive energetic systems”. In: *International Journal of Hydrogen Energy* 46.51 (July 2021), pp. 26174–26184. ISSN: 0360-3199.

[13] Parisa Mojaver et al. "Comprehensive comparison of SOFCs with proton-conducting electrolyte and oxygen ion-conducting electrolyte: Thermo economic analysis and multi-objective optimization". In: *Energy Conversion and Management* 205 (Feb. 2020), p. 112455. ISSN: 0196-8904.

[14] Meng Ni, Dennis Y.C. Leung, and Michael K.H. Leung. "Thermodynamic analysis of ammonia fed solid oxide fuel cells: Comparison between proton-conducting electrolyte and oxygen ion-conducting electrolyte". In: *Journal of Power Sources* 183.2 (Sept. 2008), pp. 682–686. ISSN: 0378-7753.

[15] Giuseppe De Lorenzo, Rosario Marzio Ruffo, and Petronilla Fragiacomo. "Preliminary Design of the Fuel Cells Based Energy Systems for a Cruise Ship". In: *World Electric Vehicle Journal* 14.9 (Sept. 2023), p. 263. ISSN: 2032-6653.

[16] L. van Biert et al. "A review of fuel cell systems for maritime applications". In: *Journal of Power Sources* 327 (Sept. 2016), pp. 345–364. ISSN: 0378-7753.

[17] Francesco Baldi et al. "The role of solid oxide fuel cells in future ship energy systems". In: *Energy* 194 (Mar. 2020), p. 116811. ISSN: 0360-5442.

[18] F Calise, M Denticedaccadia, and G Restuccia. "Simulation of a tubular solid oxide fuel cell through finite volume analysis: Effects of the radiative heat transfer and exergy analysis". In: *International Journal of Hydrogen Energy* 32.17 (Dec. 2007), pp. 4575–4590. ISSN: 0360-3199.

[19] Sunil Murthy and Andrei G Fedorov. "Radiation heat transfer analysis of the monolith type solid oxide fuel cell". In: *Journal of Power Sources* 124.2 (Nov. 2003), pp. 453–458. ISSN: 0378-7753.

[20] David L. Damm and Andrei G. Fedorov. "Spectral Radiative Heat Transfer Analysis of the Planar SOFC". In: *Journal of Fuel Cell Science and Technology* 2.4 (Apr. 2005), pp. 258–262. ISSN: 1551-6989.

[21] K.J. Daun et al. "Radiation heat transfer in planar SOFC electrolytes". In: *Journal of Power Sources* 157.1 (June 2006), pp. 302–310. ISSN: 0378-7753.

[22] X. Xue et al. "Dynamic modeling of single tubular SOFC combining heat/mass transfer and electrochemical reaction effects". In: *Journal of Power Sources* 142.1–2 (Mar. 2005), pp. 211–222. ISSN: 0378-7753.

[23] Ellen Ivers-Tiffée, André Weber, and Dirk Herbstritt. "Materials and technologies for SOFC-components". In: *Journal of the European Ceramic Society* 21.10–11 (Jan. 2001), pp. 1805–1811. ISSN: 0955-2219.

[24] Meilin Liu et al. "Rational SOFC material design: new advances and tools". In: *Materials Today* 14.11 (Nov. 2011), pp. 534–546. ISSN: 1369-7021.

[25] Yang Gao et al. "A comprehensive review of recent progresses in cathode materials for Proton-conducting SOFCs". In: *Energy Reviews* 2.3 (Sept. 2023), p. 100038. ISSN: 2772-9702.

[26] Chih-Kuang Lin et al. "Thermal stress analysis of a planar SOFC stack". In: *Journal of Power Sources* 164.1 (Jan. 2007), pp. 238–251. ISSN: 0378-7753.

[27] Kwangjin Park et al. "Fast performance degradation of SOFC caused by cathode delamination in long-term testing". In: *International Journal of Hydrogen Energy* 35.16 (Aug. 2010), pp. 8670–8677. ISSN: 0360-3199.

[28] Tao Yang et al. "Multiphysics modeling of SOFC performance degradation caused by interface delamination and active layer cracking". In: *International*

*Journal of Hydrogen Energy* 47.97 (Dec. 2022), pp. 41124–41137. ISSN: 0360-3199.

[29] Mungmuang Promsen et al. "Metallic PCM-integrated solid oxide fuel cell stack for operating range extension". In: *Energy Conversion and Management* 255 (Mar. 2022), p. 115309. ISSN: 0196-8904.

[30] Hussein Togun et al. "A critical review on phase change materials (PCM) based heat exchanger: Different hybrid techniques for the enhancement". In: *Journal of Energy Storage* 79 (Feb. 2024), p. 109840. ISSN: 2352-152X.

[31] Md. Hasan Zahir et al. "Challenges of the application of PCMs to achieve zero energy buildings under hot weather conditions: A review". In: *Journal of Energy Storage* 64 (Aug. 2023), p. 107156. ISSN: 2352-152X.

[32] Mehwish Mahek Khan et al. "Hybrid PCM-based thermal management for lithium-ion batteries: Trends and challenges". In: *Journal of Energy Storage* 73 (Dec. 2023), p. 108775. ISSN: 2352-152X.

[33] Jie Luo et al. "Battery thermal management systems (BTMs) based on phase change material (PCM): A comprehensive review". In: *Chemical Engineering Journal* 430 (Feb. 2022), p. 132741. ISSN: 1385-8947.

[34] D.S. Jayathunga et al. "Phase change material (PCM) candidates for latent heat thermal energy storage (LHTES) in concentrated solar power (CSP) based thermal applications - A review". In: *Renewable and Sustainable Energy Reviews* 189 (Jan. 2024), p. 113904. ISSN: 1364-0321.

[35] Varun Goel et al. "PCM-assisted energy storage systems for solar-thermal applications: Review of the associated problems and their mitigation strategies". In: *Journal of Energy Storage* 69 (Oct. 2023), p. 107912. ISSN: 2352-152X.

[36] Mingyang Sun et al. “A review on thermal energy storage with eutectic phase change materials: Fundamentals and applications”. In: *Journal of Energy Storage* 68 (Sept. 2023), p. 107713. ISSN: 2352-152X.

[37] Anthony Joseph Rawson et al. “Selection of compatible metallic phase change materials and containers for thermal storage applications”. In: *Journal of Energy Storage* 32 (Dec. 2020), p. 101927. ISSN: 2352-152X.

[38] Yassine El Karim et al. “Investigation of magnesium-copper eutectic alloys with high thermal conductivity as a new PCM for latent heat thermal energy storage at intermediate-high temperature”. In: *Journal of Energy Storage* 26 (Dec. 2019), p. 100974. ISSN: 2352-152X.

[39] Diana Farkas and C. E. Birchenall. “New eutectic alloys and their heats of transformation”. In: *Metallurgical Transactions A* 16.3 (Mar. 1985), pp. 323–328. ISSN: 2379-0180.

[40] Mukesh Kumar, Ravi Kant Gupta, and Anand Pandey. “Study of Cu-W, Cu-Mg, Cu-Si phase diagrams to fabricate composite electrode tool for Electrical Discharge machining”. In: *Materials Today: Proceedings* 63 (2022), pp. 422–426. ISSN: 2214-7853.

[41] P. Blanco-Rodríguez et al. “Thermophysical characterization of Mg–51%Zn eutectic metal alloy: A phase change material for thermal energy storage in direct steam generation applications”. In: *Energy* 72 (2014), pp. 414–420. ISSN: 0360-5442.

[42] Nan Sheng et al. “Macro-encapsulated metallic phase change material over 1000 °C for high-temperature thermal storage”. In: *Solar Energy Materials and Solar Cells* 239 (June 2022), p. 111655. ISSN: 0927-0248.

[43] A. Palacios et al. “A perspective on Phase Change Material encapsulation: Guidance for encapsulation design methodology from low to high-temperature thermal energy storage applications”. In: *Journal of Energy Storage* 72 (Nov. 2023), p. 108597. ISSN: 2352-152X.

[44] Ryo Fukahori et al. “Macro-encapsulation of metallic phase change material using cylindrical-type ceramic containers for high-temperature thermal energy storage”. In: *Applied Energy* 170 (May 2016), pp. 324–328. ISSN: 0306-2619.

[45] Kyung Joong Yoon, Srikanth Gopalan, and Uday B. Pal. “Analysis of Electrochemical Performance of SOFCs Using Polarization Modeling and Impedance Measurements”. In: *Journal of The Electrochemical Society* 156.3 (2009), B311. ISSN: 0013-4651.

[46] Fu Wang et al. “A comprehensive review on high-temperature fuel cells with carbon capture”. In: *Applied Energy* 275 (Oct. 2020), p. 115342. ISSN: 0306-2619.

[47] A. Gebregergis et al. “Solid Oxide Fuel Cell Modeling”. In: *IEEE Transactions on Industrial Electronics* 56.1 (Jan. 2009), pp. 139–148. ISSN: 0278-0046.

[48] J Padullés, G.W Ault, and J.R McDonald. “An integrated SOFC plant dynamic model for power systems simulation”. In: *Journal of Power Sources* 86.1–2 (Mar. 2000), pp. 495–500. ISSN: 0378-7753.

[49] K. Sedghisigarchi and A. Feliachi. “Dynamic and Transient Analysis of Power Distribution Systems With Fuel Cells—Part I: Fuel-Cell Dynamic Model”. In: *IEEE Transactions on Energy Conversion* 19.2 (June 2004), pp. 423–428. ISSN: 0885-8969.

[50] D.J. Hall and R.G. Colclaser. "Transient modeling and simulation of a tubular solid oxide fuel cell". In: *IEEE Transactions on Energy Conversion* 14.3 (1999), pp. 749–753. ISSN: 0885-8969.

[51] Elmar Achenbach. "Response of a solid oxide fuel cell to load change". In: *Journal of Power Sources* 57.1–2 (Sept. 1995), pp. 105–109. ISSN: 0378-7753.

[52] L. Barelli, G. Bidini, and A. Ottaviano. "Solid oxide fuel cell modelling: Electrochemical performance and thermal management during load-following operation". In: *Energy* 115 (Nov. 2016), pp. 107–119. ISSN: 0360-5442.

[53] Jie Yang et al. "Control-oriented thermal management of solid oxide fuel cells based on a modified Takagi–Sugeno fuzzy model". In: *Journal of Power Sources* 188.2 (Mar. 2009), pp. 475–482. ISSN: 0378-7753.

[54] D.A. Noren and M.A. Hoffman. "Clarifying the Butler–Volmer equation and related approximations for calculating activation losses in solid oxide fuel cell models". In: *Journal of Power Sources* 152 (Dec. 2005), pp. 175–181. ISSN: 0378-7753.

[55] "Chapter 2: Fuel Cell Thermodynamics". In: *Fuel Cell Fundamentals*. John Wiley & Sons, Ltd, 2016. Chap. 2, pp. 25–76. ISBN: 9781119191766.

[56] A. Virkar et al. "The role of electrode microstructure on activation and concentration polarizations in solid oxide fuel cells". In: *Solid State Ionics* 131 (2000), pp. 189–198.

[57] T V V S Lakshmi, P Geethanjali, and Prasad S Krishna. "Mathematical modelling of solid oxide fuel cell using Matlab/Simulink". In: *2013 Annual International Conference on Emerging Research Areas and 2013 International Con-*

*ference on Microelectronics, Communications and Renewable Energy*. IEEE, June 2013.

[58] Hiroyuki Shimada et al. "Challenge for lowering concentration polarization in solid oxide fuel cells". In: *Journal of Power Sources* 302 (Jan. 2016), pp. 53–60. ISSN: 0378-7753.

[59] G. D'Andrea et al. "Dynamic model with experimental validation of a biogas-fed SOFC plant". In: *Energy Conversion and Management* 135 (Mar. 2017), pp. 21–34.